Journal of Electric Propulsion

RESEARCH Open Access

Modeling grid erosion in the NEXT ion thruster using the CEX2D and CEX3D codes

James Polk[1*], Vernon Chaplin[1], John Anderson[1], John Yim[2], George Soulas[2], George Williams[2] and Rohit Shastry[2]

*Correspondence:
james.e.polk@jpl.nasa.gov

[1] Jet Propulsion Laboratory, California Institute of Technology, 4800 Oak Grove Dr., Pasadena 91109, California, USA
[2] NASA Glenn Research Center, 21000 Brookpark Rd., Cleveland 44135, Ohio, USA

Abstract

NASA's Evolutionary Xenon Thruster (NEXT) is a candidate for future deep space missions that offers high efficiency and specific impulse over a large power throttling range. One of the key life-limiting components is the ion accelerator system, which is subject to sputter erosion by low energy discharge plasma ions incident on the upstream screen grid and higher energy charge exchange ions that impact the downstream accelerator grid. The grid erosion codes CEX2D and CEX3D were validated with data from tests of NEXT as well as the NSTAR ion thruster and then used to assess the time to failure in space due to screen grid erosion and electron backstreaming caused by accelerator grid aperture erosion. Screen grid erosion was found to be important only at the lowest throttle levels, and was conservatively estimated to lead to failure after processing over 900 kg of xenon. The first failure mode at high power levels was found to be electron backstreaming due to accelerator grid hole wall erosion, which would occur after processing over 700 kg of propellant.

Keywords: Electric propulsion, Ion thrusters, Ion optic modeling, Grid erosion

Introduction

NASA's Evolutionary Xenon Thruster (NEXT) and the associated power processing unit, propellant management assembly, and gimbal were developed to support ambitious future deep space and commercial missions. NEXT employs two-grid, outward-dished ion optics and can be throttled from 0.5-6.9 kW input power to accommodate variations in solar array output with solar range. It produces thrust values from 25-237 mN and specific impulses from 1300-4150 seconds. Throttling is accomplished by varying beam voltage and current over 40 discrete throttle levels (TLs) [1], as displayed in Fig. 1. The NEXT ion propulsion system is being demonstrated on the Double Asteroid Redirect Test (DART) mission, which was launched in 2021. [2]

Grid structural failure and electron backstreaming due to sputter erosion are key potential failure modes. The modeling of these processes described in this paper is being used in conjunction with wear testing to establish engine service life, in accordance with NASA recommendations for life qualification [3, 4]. We employed the Jet Propulsion Laboratory's CEX2D and CEX3D codes, which are two- and three-dimensional models

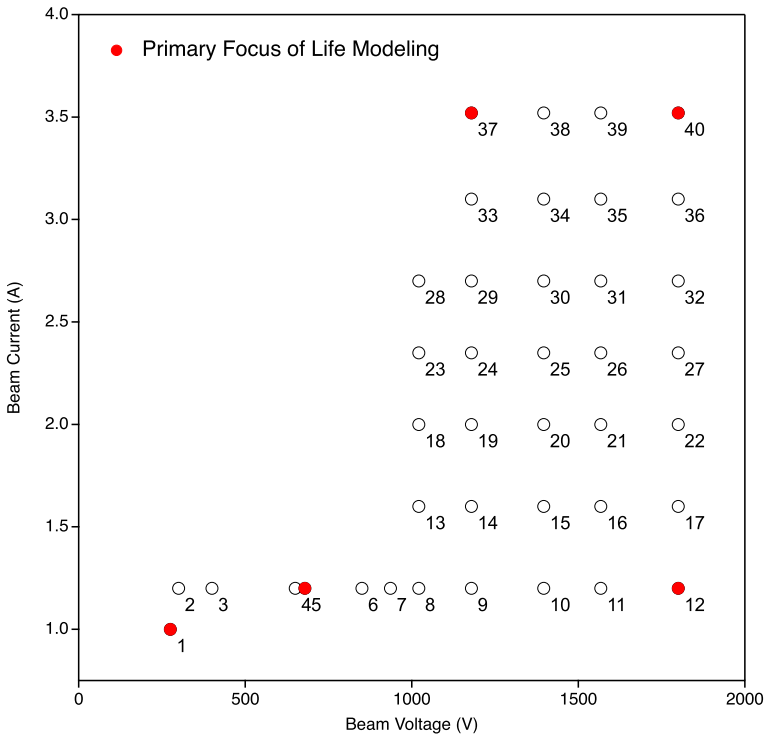

Fig. 1 NEXT throttling envelope in terms of beam voltage and current. 40 discrete throttle levels allow operation over an input power range of 0.5 to 6.9 kW. Throttle levels (TLs) 1, 5, 12, 37, and 40 shown in red are the focus of the erosion simulations

of individual ion beamlets that simulate the primary ions, the neutral gas flow from the engine and the ambient neutral gas, charge exchange reactions between primary ions and neutrals, and the sputter erosion of the grids by thruster and charge exchange ions. The specific objectives of the work reported here were to validate the codes and use them to predict erosion for in-space conditions. The primary focus was on the five throttle points shown in red in Fig. 1, which represent extremes in currents or voltages that can result in worst case erosion rates. We report the results for screen grid erosion and electron backstreaming due to accelerator grid aperture wall erosion. Modeling of the erosion in the pits and grooves pattern that forms on the downstream face of the accelerator grid was reported in an earlier paper [5]. The results presented here are deterministic predictions of time to failure in space, based on nominal code input parameters. A preliminary probabilistic analysis of electron backstreaming failure that incorporates the variability in some of the input parameters is discussed in [6].

A key part of the testing that complements the modeling work reported here was the NEXT Long-Duration Test (LDT). The test article was a modified version of an engineering model (designated EM3) which incorporated prototype-model (PM) ion optics and a graphite discharge cathode keeper electrode. More detailed descriptions of the hardware and the vacuum facility can be found elsewhere [7–12]. The thruster was operated over a range of throttle levels representative of candidate mission profiles [13] for the first 29,000 hours and then at full power for a total of 51,184 hours [14]. The operating conditions, which match the five throttle levels highlighted in Fig. 1, are summarized

Table 1 Operating conditions for the next long duration test segments

Throttle Level (TL)	Thruster Power (kW)	Beam Current and Voltage	Segment Duration (hrs)	Cumulative Duration (hrs)	Segment Throughput (kg)	Cumulative Throughput (kg)	Backsputter Rate (μm/kh)
40	6.9	3.52 A, 1800 V	13,042	13,042	264.7	264.7	2.8
37	4.7	3.52 A, 1179 V	6,478	19,520	132.6	397.3	1.2
5	1.1	1.20 A, 679 V	3,411	22,931	26.7	424.0	0.2
1	0.5	1.00 A, 275 V	3,198	26,129	23.4	447.4	0.1
12	2.4	1.20 A, 1800 V	3,111	29,240	24.5.	471.9	1.0
40	6.9	3.52 A, 1800 V	21,944	51,184	446.3	918.2	2.8

in Table 1. A total of 918 kg of propellant was processed, demonstrating a total impulse of 35.5 MN-s.

The NEXT LDT was conducted in a vacuum facility at the NASA Glenn Research Center (GRC) which incorporates a graphite beam target to minimize backsputtering. Despite this, carbon backsputter rates of up to 2.8 μm/kh were measured in the LDT, as shown in Table 1. As a result, carbon deposits up to 70% of the accelerator grid thickness accumulated on the ion optics, making interpretation of the erosion difficult. The CEX2D and CEX3D models were also used to determine how carbon deposition during the test influenced the wear rates and determine which results could be reliably used to help validate the models.

The CEX2D and CEX3D codes

CEX2D [3, 15, 16] models an axisymmetric beamlet and charge exchange ions in cylindrical coordinates. It is used primarily to model screen grid and accelerator hole wall erosion, processes which are well represented by an axisymmetric approximation. CEX3D [5, 17] uses Cartesian coordinates and simulates a triangular wedge spanning 1/12 of the beamlet as shown in Fig. 2. This is the minimum domain necessary to capture the 3D beamlet properties, taking advantage of the hexagonal symmetry of the grid hole pattern [18]. CEX3D is used to model the inherently three dimensional pits and grooves erosion on the downstream face of the accelerator grid and certain aspects of accelerator hole wall erosion, such as the effect of carbon deposition on net erosion rate. The computational mesh in CEX3D is made up of 30-60-90 triangular prisms with constant transverse dimensions dx and dy. The mesh in CEX2D consists of rectilinear elements with constant radial dimensions dr. Both codes use variable axial mesh spacing dz, with progressively larger mesh volumes in the region downstream of the grids where the ion density is low.

The codes consist of separate modules that solve for the primary beam ion trajectories, the neutral gas density distribution, charge exchange ion formation and motion, and sputter erosion, as outlined in Fig. 3. The beam and neutral gas models provide the inputs needed for the charge exchange ion model, and grid erosion due to discharge plasma ions, beamlet ions, and charge exchange ions is calculated.

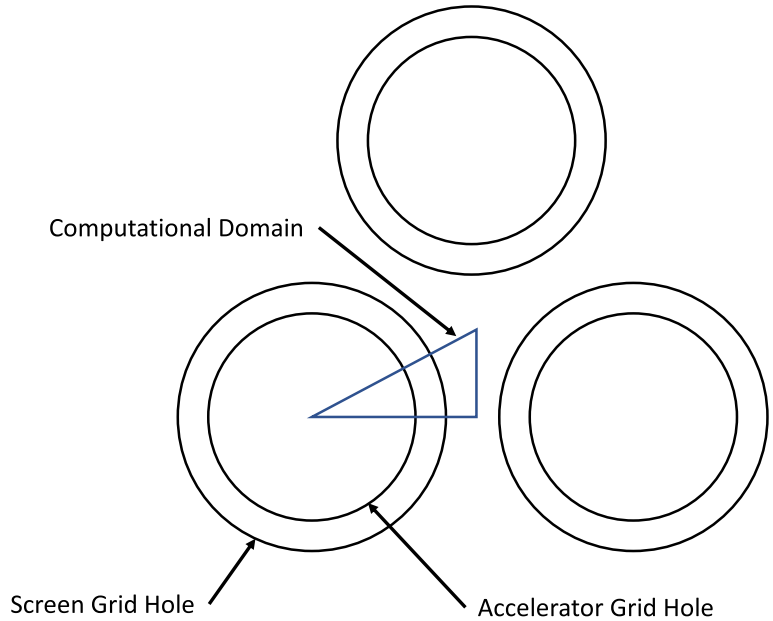

Fig. 2 The computational domain of CEX3D is a triangular prism representing 1/12 of an aperture in the hexagonal pattern

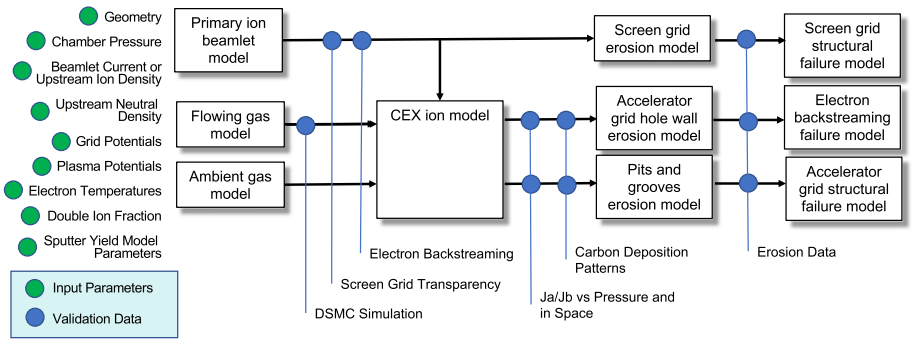

Fig. 3 Schematic of the CEX2D and CEX3D codes. The boxes represent individual code modules, the green circles indicate input parameters, and the blue circles show where experimental data can be compared to module outputs for validation

CEX2D can simulate time-dependent erosion [16] in which the particle trajectories and potential are updated as the grid geometry changes.

Ion beamlet model

Both codes use a "flux tube" approximation [18, 19] for the beam ion solution. Macroparticles are pushed through a static potential with charge density assigned to each mesh node in proportion to the time each macroparticle spends in its vicinity, then the potential solution is updated and the process is repeated until convergence. The beam ion macroparticles enter the domain at the upstream boundary with uniform number density and axially directed Bohm velocity. The more mobile electrons are assumed to follow a Boltzmann density distribution as a function of the local

potential. Plasma density is specified on the upstream boundary and the electron density is assumed to be zero between the downstream face of the screen grid and the axial location of the potential minimum. Uniform electron temperatures are specified for the upstream and downstream plasmas. A linearized version of Poisson's equation [5] is solved with constant (Dirichlet) boundary conditions at the upstream and downstream edges of the domain, and zero derivative (Neumann) boundary conditions at the symmetry boundaries. Macroparticles that contact the grids or cross the upstream or downstream boundaries are removed from the simulation, while those incident on other boundaries are specularly reflected, simulating an ion from an adjacent beamlet (or from another part of the same beamlet in the case of CEX3D) entering the domain while the original ion exits.

Neutral gas models

The neutral gas density due to flow through the grids is modeled by treating the downstream boundary of the accelerator grid hole as a disk-shaped particle sink on the upstream side and as an effusive particle source on the downstream side [5, 20]. The flow rate is equal to the thermal flux at the specified upstream neutral density (with a gas temperature based on the discharge chamber wall temperature) scaled by a Clausing factor calculated using a Monte Carlo simulation for an approximate grid geometry. The velocity distribution is represented by a drifting Maxwellian with a mean velocity obtained from the Clausing factor calculation. We set the gas temperature downstream of the grids to be 2/3 of the discharge chamber gas temperature based on typical results from the higher fidelity 3D Monte Carlo simulation described below, which shows gas cooling due to expansion.

The contribution to the neutral density due to ambient gas in ground test facilities is calculated from the measured pressure and modeled using two distribution functions; one for the population flowing toward the grids and one for the population reflected from the accelerator grid. The population flowing toward the grids is assumed to have a 300 K half-Maxwellian velocity distribution in the axial direction and 300 K full Maxwellian distribution in the other two directions, with density equal to half of the background neutral density. All of the incident neutrals are assumed to scatter off of the accelerator grid after full accommodation, with a half-Maxwellian velocity distribution at the grid temperature in the axial direction and a full Maxwellian distribution at this temperature in the other two directions. The density of the outflowing background population is chosen to make the flux of gas toward and away from the thruster equal (i.e., ingestion of some incident gas through the grids into the discharge chamber is neglected). In the NEXT and NSTAR tests the pressure was measured using an ionization gauge located next to the thruster at a radius of 0.5 m [21]. Although the pressure varies throughout the test chamber, this measurement is the best available characterization of the near-field pressure which influences grid erosion.

Charge exchange ion model

In CEX2D and CEX3D the charge exchange ion birth rate per unit volume is calculated from the beam ion density, the neutral gas density, the charge exchange reaction cross sections, and the beam ion velocity. The beam ion density and neutral gas density

distributions are treated as static because only a small fraction of beam ions and neutrals undergo charge exchange reactions as they transit the simulation domain. The charge exchange cross sections for the symmetric processes $Xe^{n+}+Xe \rightarrow Xe + Xe^{n+}$ ($n = 1$ or 2) are calculated using formulas developed by Miller [22] from measured cross sections, and the energy and velocity of beam ions are calculated from the beamlet potential solution using energy conservation [5].

CEX2D pushes charge exchange ion macroparticles through a static beamlet potential distribution. Neglecting the space charge due to charge exchange ions has little impact on hole wall erosion, because beam ion contributions to the potential dominate in the non-neutral region very near the accelerator grid where the ions that impact the hole walls are born. On the other hand, charge exchange ions that cause pits and grooves erosion can be born far downstream (several cm) of the grid, and the perturbations to the potential in this region caused by their space charge, while small ($\ll$10 V), can have an important effect on both the total flux and spatial distribution of charge exchange ions striking the accelerator grid. Therefore, CEX3D employs a full particle-in-cell (PIC) [23] model for the charge exchange ions and self-consistently calculates the potential due to the total space charge [5].

In CEX2D the initial velocity of each charge exchange ion is assumed to be equal to the mean velocity of the neutral gas flow downstream of the grids. Because of the large potential gradients near the grids, the trajectories of charge exchange ions that strike the accelerator grid hole wall are not particularly sensitive to the assumed initial velocity. However, the trajectories of charge exchange ions created far downstream that impact in the pits and grooves pattern are more sensitive to the initial velocity. CEX3D therefore incorporates a more detailed model that randomly selects the charge exchange ion velocity component in each direction from a distribution that accounts for both the finite temperature of the gas and the non-zero momentum transfer in charge exchange collisions [24–26]. The code includes velocity rescaling for the slow charge exchange ions to allow larger time steps, as described in detail by Chaplin [5].

Grid erosion model

When an ion macroparticle strikes a grid, it is removed from the computation and the sputtered grid mass is calculated using the semi-empirical formula for yield at normal incidence developed by Eckstein [27]. The variation in yield with ion angle-of-incidence is calculated using the Wei formula [28]. CEX2D corrects the grid erosion rates for the presence of doubly-charged ions [5, 16]. This correction is required to accurately calculate the screen grid erosion rate from incident discharge chamber ions, due to the very strong energy dependence of the sputtering yield at low energies [29] and the relatively high double ion content of the discharge plasma. The double ion content of the charge exchange ions which strike the downstream face of the accelerator grid is lower because of the difference in charge exchange cross sections for double and single beam ions. These ions also bombard the grid at higher energies, so the difference in yield for double and single ions is not as high. As a result, the error in the pits and grooves erosion rate is negligible and double ions are not accounted for in CEX3D. For example, assuming a ratio of double-to-single ion current of 10% and a single ion energy of 250 eV, which are

typical values for these parameters, the error in treating all of the current as single ions is less than 4%.

In order to follow the time evolution of the grid geometry, CEX2D keeps track of the mass on each mesh node, which is reduced each time there is a sputtering event. Nodes within the grid are fixed at the grid potential until their mass reaches zero, at which time they are re-classified as free space nodes and the potential is updated according to Poisson's equation. Because the potential is not updated until a cell is completely removed, sudden jumps of a few volts in the calculated electron backstreaming limits can occur. As the grid shape evolves in time, the direction of the surface normal at each location, which is required for the sputtering calculation, is approximated by the vector from the local center of mass to the center of the surface edge [30].

A significant fraction of the ions sputtered from the accelerator grid aperture wall will be redeposited elsewhere on the wall, reducing the net erosion rate. Simulations show that most of the ions strike the wall with close to normal incidence because of the potential structure in the aperture. Measurements of the differential sputter yield for xenon on molybdenum demonstrate that the sputtered atom flux is strongly peaked at an angle of 60 degrees from the surface normal for normally incident ions at energies ranging from 75 to 750 eV [31, 32]. This behavior is exploited to estimate an average value for the redeposited fraction by approximating the accelerator grid hole as a perfect cylinder, assuming sputtering occurs uniformly over the surface, and assuming all sputtered atoms are emitted at an angle of 60 degrees. For the NSTAR and NEXT aperture geometry this approach yields a redeposited fraction of 0.4, so the mass loss rate of the accelerator grid is reduced by this amount in CEX2D. CEX3D does not account for redeposition; time-dependent pits-and-grooves erosion and redeposition are simulated in a separate code with inputs from CEX3D.

Electron backstreaming model

Electron backstreaming occurs when the magnitude of the negative potential inside the accelerator grid holes becomes small enough that a non-negligible current of plume electrons can flow upstream through the grids. Electron backstreaming reduces the thruster's electrical efficiency and can produce unacceptably high heat loads in the discharge chamber, thus ending the useful life of the engine. CEX2D calculates the electron backstreaming current by integrating the electron flux over a surface defined by the minimum potential inside the accelerator grid hole as a function of radius [15].

In order to calculate the electron backstreaming limit V_{EBS}, CEX2D reduces the magnitude of the accelerator grid voltage in one volt steps until electron backstreaming occurs. In this work, V_{EBS} for a single beamlet is defined to be the accelerator grid voltage V_a at which the electron backstreaming current is 1% of the beamlet current. Changing this threshold to 0.1% or 10% would only change the calculated electron backstreaming limit by a few volts because of the exponential dependence of the electron backstreaming current on potential. This exponential growth of electron backstreaming current with V_a also implies that once the electron backstreaming current threshold has been exceeded for beamlets at some radial location on the grid, the accelerator grid voltage will need to

be increased only slightly for the electron backstreaming threshold for the entire beam to be exceeded. Therefore, for these simulations we make the approximation that the most negative electron backstreaming limit calculated for any single beamlet on the grid is equal to the overall electron backstreaming limit for the thruster.

Code verification

The simulation input parameters and the code algorithms were tested to verify that the physics models described above were properly implemented. For example, a revised calculation correcting for the effect of grid curvature on the axial potential gradient in the beam was verified by showing that the results obtained with beam ions alone matched the analytical result of a Boltzmann relation dependence on ion density [5]. Parametric studies verified that the choices for the following parameters were not affecting the results:

- Mesh resolution
- Beam ion and charge exchange ion macroparticle size (i.e., the number of macroparticles in the calculations)
- Particle pushing time step
- Simulation domain length
- CEX3D PIC simulation runtime (verifying that the potential solution and the accelerator grid current reached a steady state)
- Threshold for rescaling PIC ion velocity [5]

Model validation

As part of this work we compared predicted screen grid and accelerator grid hole wall erosion rates with erosion measurements to validate the primary code outputs, as well as measurements of intermediate quantities to validate individual code modules, as shown in Fig. 3. These included measurements of electron backstreaming voltage and screen grid transparency, which test the primary ion model, and carbon deposition patterns from ground testing, which test the charge exchange ion models. Some components, such as the neutral gas model, are difficult to validate because there are no detailed measurements. In this case we used a higher fidelity direct simulation Monte Carlo (DSMC) code to validate the model used in the ion optics codes.

The validation data were from four tests of two different thrusters–the 8200 hour test of an engineering model NSTAR thruster (the NSTAR LDT), the 30,352 hour Extended Life Test (ELT) of the Deep Space 1 flight spare NSTAR engine, a 2000 hour test of a laboratory model (LM) NEXT thruster, and the 51,184 hour NEXT LDT. The data sets consisted of beginning-of-life (BOL) screen grid transparency and electron backstreaming voltage measurements over a range of throttle levels, variations in electron backstreaming voltage during the wear tests, and in situ and post-test measurements of screen grid and accelerator grid aperture erosion patterns.

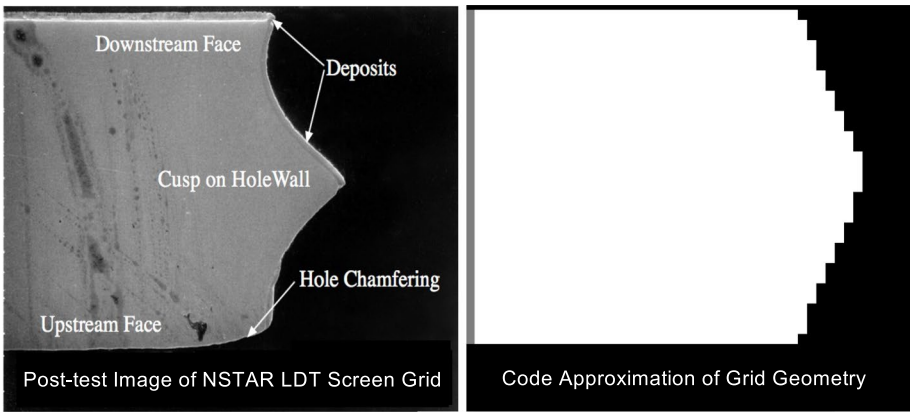

Fig. 4 Cross section of screen grid showing cusped geometry and idealized code geometry which approximates the cusp shape

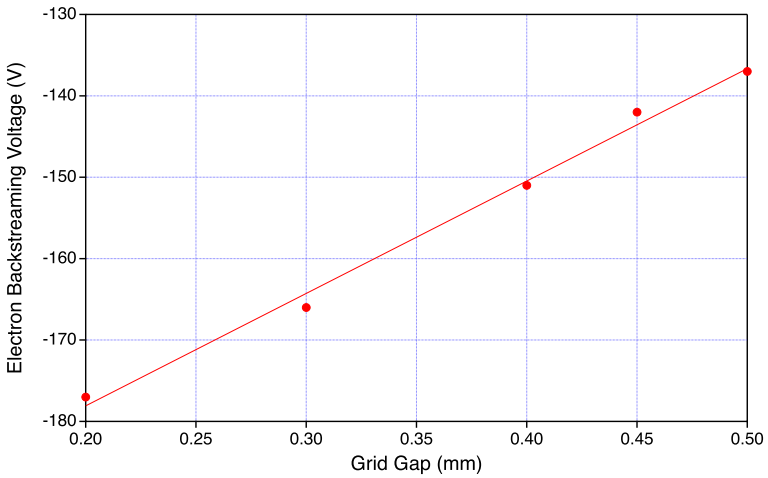

Fig. 5 Electron backstreaming voltage predicted by CEX2D simulations for the NSTAR LDT test conditions, beginning-of-life aperture geometry, and a range of hot grid gaps. These results show that the measured backstreaming voltage can be a sensitive indicator of the hot gap

Input parameters for the validation cases

The validation also included a critical assessment of the input parameters' pedigree. Key input parameters shown on the left in Fig. 3 include the optics geometry, the thruster component potentials, discharge chamber and beam plasma properties, and neutral gas properties. The sources of data used to define these parameters are summarized in Appendix A Sources of data for model inputs.

The codes approximate the cusped geometry of the grids as shown in Fig. 4. Grid thickness and aperture diameters were based on pre-test measurements where available, post-test measurements if they were considered a reliable estimate of the initial conditions, or the design specification. The radius of curvature of the dished grids and the beam diameter in all simulations were based on the manufacturing specification. Details of pre- and post-test measurements for these tests are available in the references listed in Appendix A Sources of data for model inputs.

The grid gap when the grids are hot is a key geometric parameter, particularly for electron backstreaming calculations, and is one of the most difficult to measure. For the NSTAR cases we performed a parametric study the effect of grid gap on BOL electron backstreaming voltage for the NSTAR LDT, as shown in Fig. 5. The backstreaming voltage is a sensitive indicator of grid gap, and the value for the hot gap that produced the best agreement with the measured backstreaming voltage at BOL (0.45 mm) also reproduced the measured changes in backstreaming voltage over the course of the test, as shown in Accelerator grid erosion and electron backstreaming model validation section. This value is somewhat larger than that measured in an NSTAR LM thruster at full power by monitoring the motion of a ceramic pin that was attached to the center screen grid aperture and protruded through the accelerator grid aperture [33]. The grid gap inferred from the NSTAR LDT BOL backstreaming voltage was also used in the ELT simulations for the first test segment and yielded good agreement with the data. For subsequent test segments a slightly smaller gap matched the data well, which is consistent with post-test measurements showing a cold gap which was smaller than the pre-test cold gap [34]. The hot grid gap in the NEXT simulations was based on optical measurements obtained during the LDT [35].

The beam and accelerator grid voltages in the simulations were set equal to those measured in the wear tests. The discharge voltage was based on either average values for a given test segment (NSTAR) or the BOL values (NEXT tests). The beamlet current, which is a model input for CEX2D, was based on Faraday probe measurements in the plume near the grids. The measured beam current densities were extrapolated back to the grid surface and converted to individual beamlet currents [14, 15, 36–38]. CEX3D requires the upstream plasma density as an input. In the simulations for these cases the plasma density corresponding to a given beamlet current in CEX2D was used and the output of CEX3D was checked to verify that it produced the desired beamlet current. The upstream plasma potential was assumed to be equal to the sum of the beam voltage and the discharge potential. Emissive probe measurements in NSTAR and NEXT thrusters showed that the plasma potential near the grids was within ± 1 V of this sum [39, 40]. The upstream electron temperature was assumed to be 5 eV for all simulations. Langmuir probe measurements in an NSTAR LM thruster yielded temperatures of 3 - 5 eV [39] and 4 - 6 eV in a NEXT LM thruster [40]. Sensitivity tests showed that code results were not particularly sensitive to the upstream temperature. The screen grid erosion is strongly influenced by the double ion content of the plasma, however. In all cases the double-to-single ion current ratio was based on ExB probe measurements conducted on LM or EM thrusters [15, 41, 42].

The downstream plasma potential input was based on emissive probe measurements in the near-field plume, which generally yielded values of 13 -15 V relative to neutralizer cathode common [36, 41, 43]. For the NSTAR cases we used a downstream electron temperature of 1.8 eV based on measurements from the plasma diagnostics package on the Deep Space 1 mission [44]. For the NEXT cases we used 2 eV, assuming that it would be similar to the NSTAR electron temperature.

The average neutral density $\bar{n}_0$ in the discharge chamber is calculated by equating the free molecular flow through the grids to the neutral flow calculated from the beam current J_b and discharge propellant utilization efficiency η_{ud}. This yields

$$\bar{n}_0 = \frac{4J_b}{\bar{v}_{\mathrm{th}} A_g \phi_a K e} \frac{(1-\eta_{\mathrm{ud}})}{\eta_{\mathrm{ud}}}, \tag{1}$$

where $\bar{v}_{\text{th}} = \sqrt{8kT/\pi m}$ is the thermal velocity, k is Boltzmann's constant, T is the gas temperature, m is the xenon atom mass, A_g is the active grid area, ϕ_a is the accelerator grid transparency to neutrals, $K \approx 0.5$ is the Clausing factor for flow through the grids, and e is the electron charge. The average neutral density was used for all simulations. As shown in section Accelerator grid erosion and electron backstreaming model validation, the assumption of a uniform upstream neutral density produces good agreement with data, but this parameter should be considered relatively uncertain compared to other input parameters. It is a reasonable approximation for the NEXT thruster, which has a relatively flat beam profile. In the NSTAR thruster, however, the magnetic field design results in a high density of primary electrons on the thruster centerline which could deplete the neutral gas along the axis by ionization. The actual distribution of neutral density across the grid face is not well known. Spectroscopic measurements in an NSTAR LM thruster suggest that the density on centerline is on the order of 2.25 times lower than the average density near the grids [45]. However, estimates of the mass loss per hole from the NSTAR LDT accelerator grid based on detailed measurements of the erosion pattern [41] do not show a suppression of erosion compared to the beamlet current on the centerline that would be expected if the neutral density was lower than average there (Fig. 6).

The contribution to neutral gas densities from residual xenon gas in the vacuum test facility is based on measured pressure. As noted in section Neutral Gas Models, the chamber pressure in these tests was measured close to the thruster, so it is representative of the local environment. The ambient neutral gas populations treated in the codes are assumed to have velocities determined by thermal accommodation with the discharge chamber, the accelerator grid, or the vacuum chamber wall. The vacuum chamber was assumed to be room temperature, and the component temperatures were based on NSTAR and NEXT thermal characterization tests [46, 47].

One of the most important inputs is the set of parameters used to model the sputter yield dependence on ion energy and incidence angle. The parameters we used are based on the curve fits to data for xenon ions on molybdenum by Yim [29]. The data for sputter

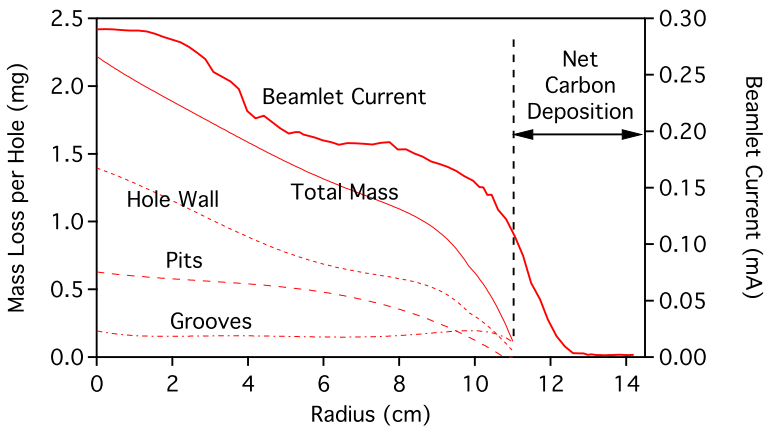

Fig. 6 The accelerator grid radial mass loss distribution compared to the beamlet current density distribution for the NSTAR LDT. The grid erosion scales roughly with current density and does not appear to be depressed in the center due to lower neutral density

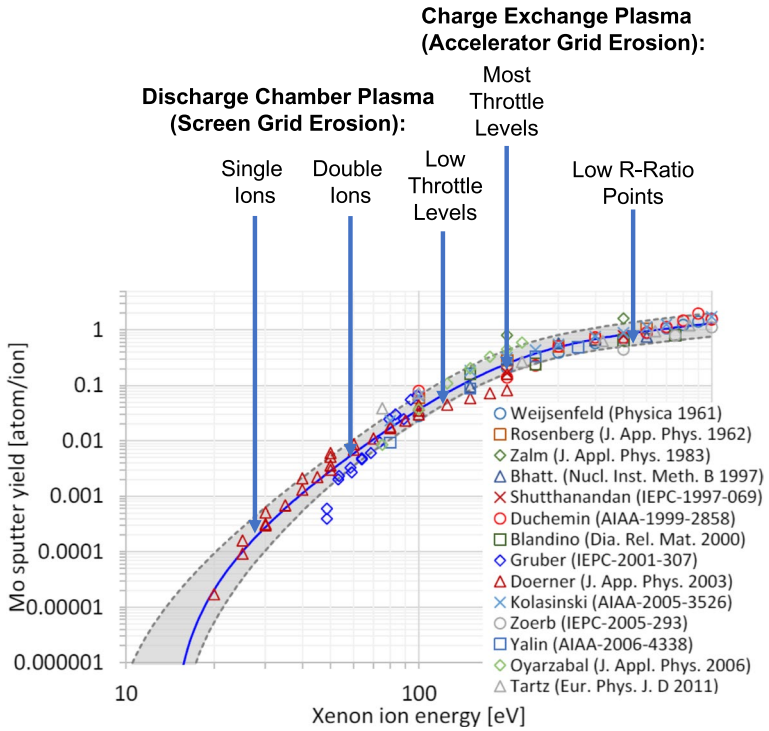

Fig. 7 Curve fits to sputter yield data for xenon on molybdenum, reproduced from Yim [29]. The solid line represents the maximum likelihood estimate and the dashed lines represent the 50% likelihood curves. The annotations indicate the energy ranges of most importance for the modeling reported here

yield at normal incidence as a function of energy from Yim's review are shown in Fig. 7. The single and double ions that impact the screen grid have energies on the order of 25 and 50 eV, respectively. As shown in Fig. 7, there are very little data in this region and the uncertainties are very large. For the screen grid erosion calculations we used the maximum likelihood curve fit (the solid line). The charge exchange ions striking the accelerator grid have minimum energies on the order of one hundred to several hundred eV. There are more data in this range, but the values are scattered. We found that the lower 50% likelihood curve (the lower dashed boundary) produced the best agreement with data for the NSTAR and NEXT tests. The maximum likelihood values for the parameters in the Wei angular dependence model were used for all simulations.

Neutral gas model validation

There are no detailed data that can be used to validate the neutral flow model because it is extremely difficult to directly measure the neutral gas flow through the grids. Instead, we used the high fidelity Direct Simulation Monte Carlo (DSMC) Analysis Code (DAC) to compare with our algorithm. This state-of-the-art tool developed by NASA is used to simulate a broad range of rarified gas dynamics problems and has been extensively validated against other DSMC codes as well as data [48]. We modeled the neutral flow through four holes in a 3D simulation with DAC using the NEXT beginning of life aperture geometry as a test case. The upstream parameters and the grid temperatures

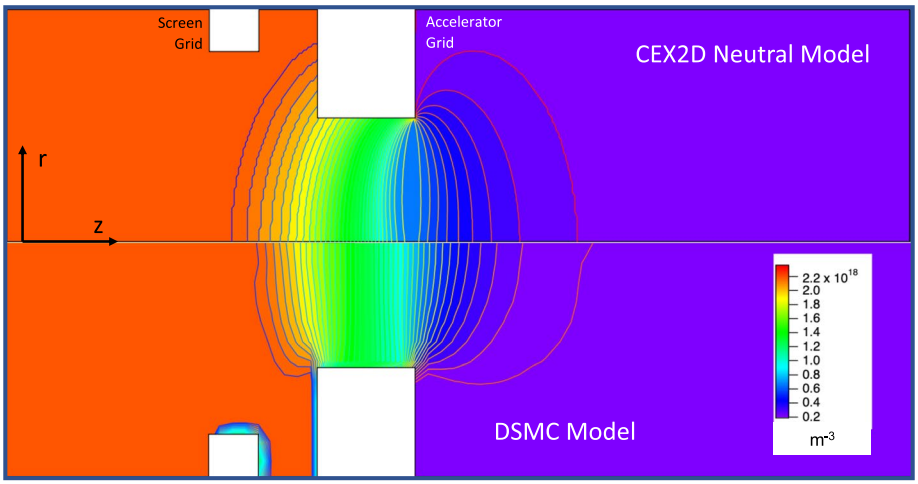

Fig. 8 The neutral density for a single aperture as a function of radial and axial position. The CEX2D neutral model results are plotted above the aperture centerline and the results from the more accurate DSMC computation are plotted below the centerline. The features in the DSMC results near the grids are an artifact of the grid resolution and how solid surfaces are modeled

matched those used in CEX3D. The results of the DAC simulation and the CEX3D results are compared in Fig. 8. The contour levels are set to the same values and show the same qualitative behavior. In certain regions such as the exit plane of the accelerator grid aperture the results differ by as much as 20%. Comparisons between grid erosion simulations using the DSMC and CEX2D neutral distributions show that these differences have negligible impact on the results because very few charge exchange ions created in these regions impact the grids.

Screen grid erosion model validation

The screen grid erosion model was validated using screen grid transparency measurements and erosion data from the NSTAR and NEXT wear tests. The grid transparency comparisons test the validity of the upstream plasma and primary beam ion models, while the erosion comparisons test the distribution of ion fluxes on the webbing and the sputtering model.

The screen grid transparency ϕ_s is the fraction of total ion current that is extracted into the beam,

$$\phi_s = \frac{J_b}{J_b + J_s}, \tag{2}$$

where J_b is the beam current and J_s is the screen grid current. CEX2D was used to calculate the average grid transparency for a range of beamlet currents at several NEXT throttle levels. The transparency calculated for the peak beamlet current was within 1% of the average transparency, so simulations for the peak beamlet current over a much broader range of throttle levels were run. The left-hand plot in Fig. 9 compares the calculated transparencies to the values measured at the beginning of the NEXT LDT. The right-hand plot displays the measured screen grid currents and the simulated values scaled

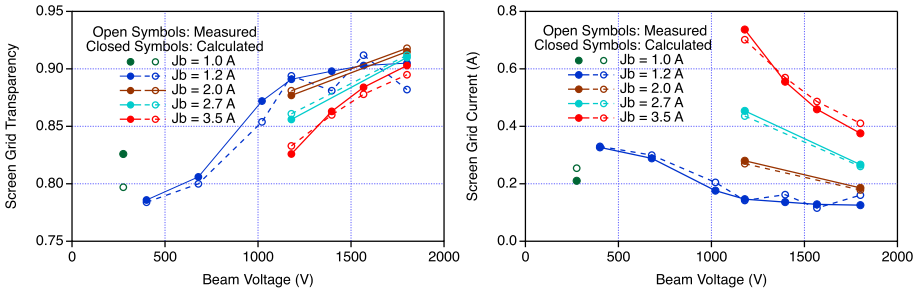

Fig. 9 Measured and calculated screen grid transparency (left) and corresponding screen grid currents (right) for points spanning the NEXT throttle table. The uncertainties in the current and transparency measurements are ± 1% and 1.5%, respectively. The code reproduces the measured values to within about 5%

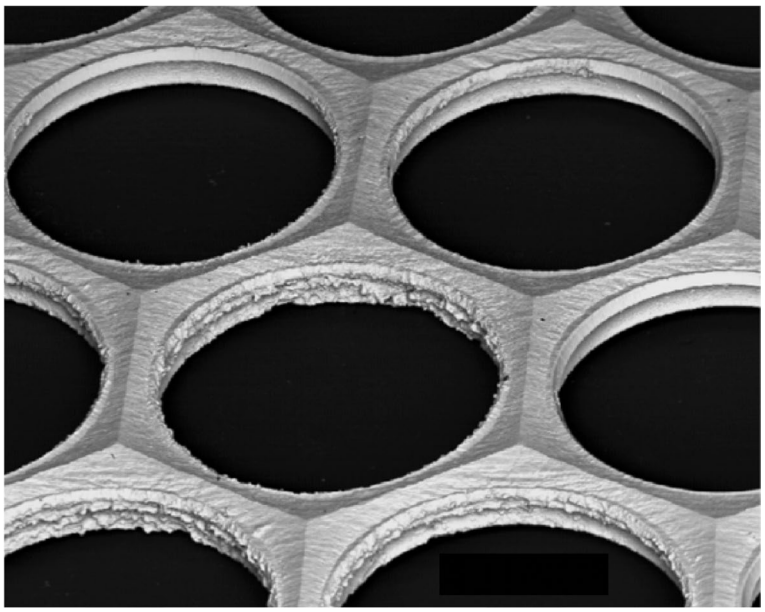

Fig. 10 Upstream surface of the screen grid from the NSTAR LDT showing the erosion pattern after 8200 hours of operation. Erosion is highest near the hole edge and lowest in the center of the webbing, leaving a hexagonal ridge between apertures

with the total beam current. The code reproduces the measured screen grid currents to within about ±5% over a large range.

Erosion on the upstream surface of the screen grid is typically highest at the hole edge and lowest in the center of the webbing, leaving a ridge between apertures as shown in a scanning electron microscope (SEM) image of a section of the screen grid from the NSTAR LDT in Fig. 10.

The ridge height varies between the thinnest part of the webbing and the region between any three holes, and the hole edge thickness is slightly different from one side of the aperture to the other because the beamlets are off-center slightly. The CEX2D code will not capture the three dimensional variations in grid thickness, but it should produce a reasonable estimate of the average erosion profile. Figure 11 shows measured edge and ridge erosion as a function of grid radius compared to CEX2D predictions.

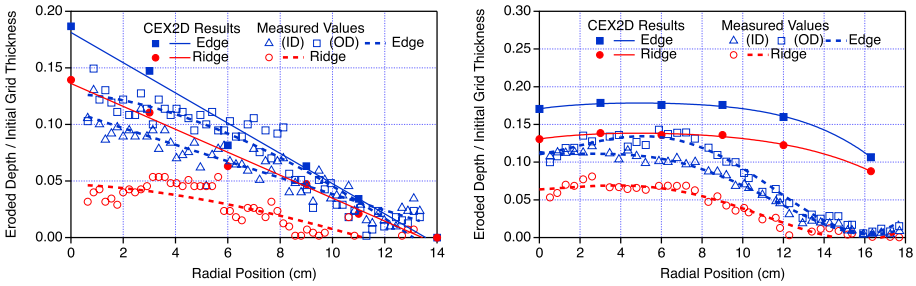

Fig. 11 Comparisons of calculated screen grid erosion and post-test measurements from the NSTAR LDT (left) and the NEXT LDT (right) show that the code tends to overpredict the erosion rate. The uncertainty in the measurements is ±3%

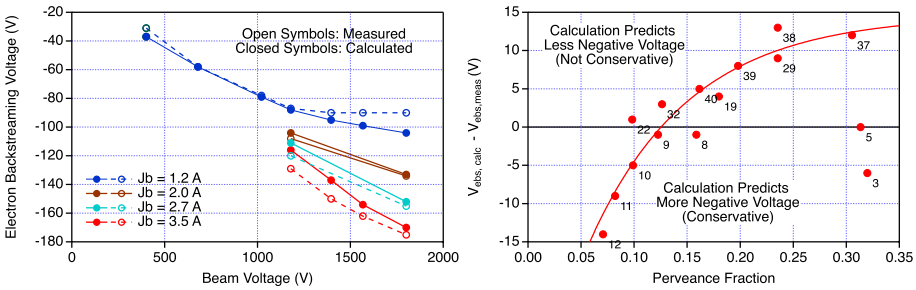

Fig. 12 Comparisons of calculated electron backstreaming voltages and measurements from the beginning of the NEXT LDT (left) show that the code reproduces measured values to within about ±15 V. The difference in measured and calculated backstreaming voltage as a function of perveance fraction plotted on the right indicates that the discrepancy scales with perveance. Numbers next to the points are the throttle levels. The uncertainty in the electron backstreaming voltage measurements is ±2.5 V

The data marked "ID" represent measurements on the side of the aperture closest to the grid center, while those labelled "OD" are on the opposite side of the aperture. For the NSTAR case shown in the left panel, the code results agree well with measured edge erosion at large grid radii, but overpredict erosion in the center by about 50%. The ridge erosion rate is overpredicted by a factor of 2 - 3 over the entire grid. The errors in calculated screen grid currents are small, so these discrepancies indicate small model errors in the ion current distribution around the hole (resulting in slightly more uniform erosion) and suggest a lower sputter yield than the value used in the model or errors in yield as a function of incidence angle. This would not be surprising, given the large uncertainties in yield near threshold. The NEXT case in the right panel shows a similar overprediction by a factor of 2 - 3 over most of the grid, with worse agreement at the grid edges. These results suggest that the double ion fraction may have been lower at the beam edges in this test than the measurements from the EM thruster [42]. In general, however, these comparisons show that the rates predicted by CEX2D are conservative.

Accelerator grid erosion and electron backstreaming model validation

The screen grid transparency comparisons described above test the validity of the primary ion beamlet model and show very good agreement. In this section, we compare measurements of electron backstreaming voltage with CEX2D predictions, which tests the beamlet model, potential solver, and electron backstreaming algorithm. In addition,

we compare the code results with measurements of hole erosion and how the electron backstreaming voltage changes with time as a result, which validates the charge exchange ion generation, trajectory tracking, and sputtering models.

The electron backstreaming voltages measured over a large range of throttle levels at the beginning of the NEXT LDT are plotted on the left side of Fig. 12 with the corresponding CEX2D predictions. The code results agree with the measurements to within ±15 V over the entire range. The plot on the right in Fig. 12 shows that, with the exception of the two lowest voltage throttle points, the difference between the measurements and calculations is correlated with the perveance fraction,

$$P = \frac{J_{\text{beamlet}}}{J_{\text{beamlet,max}}} = \frac{J_{\text{beamlet}}}{A_s \phi_s j_{\text{max}}}, \tag{3}$$

where J_{beamlet} is the beamlet current, $J_{\text{beamlet,max}} = A_s \phi_s j_{\text{max}}$ is the beamlet current at the perveance limit, based on the screen grid area associated with a single aperture A_s, transparency ϕ_s, and space charge-limited current density $j_{\text{max}} = 4.75 \times 10^{-9}(V_b - V_a)^{3/2}/l_e^2$. The space charge-limited current depends on the beam voltage V_b, the accelerator grid voltage V_a, and the effective grid gap $l_e = [(l_g + t_s)^2 + d_s^2/4]^{1/2}$, where l_g is the actual grid gap, t_s is the screen grid thickness, and d_s is the screen grid aperture diameter. This correlation suggests that the discrepancy is due to small modeling errors in the structure of the primary ion beamlet, which lead to predictions of less negative voltage required to prevent backstreaming at the highest perveance fraction conditions and more negative voltage at the lower perveance fraction points. The code predictions are therefore not conservative for high perveance fractions, so additional margin should be applied. In principle, this correlation could be used to correct the code outputs, yielding agreement to within about ±5 V, but this was not done in this study.

The time-dependent erosion simulation qualitatively reproduces the erosion profile measured in the NSTAR LDT, as shown in Fig. 13. The left image shows the outline of the grid cross section from CEX2D, while the photo on the right displays an actual cross section of the center hole from the test. The code accurately predicts that the

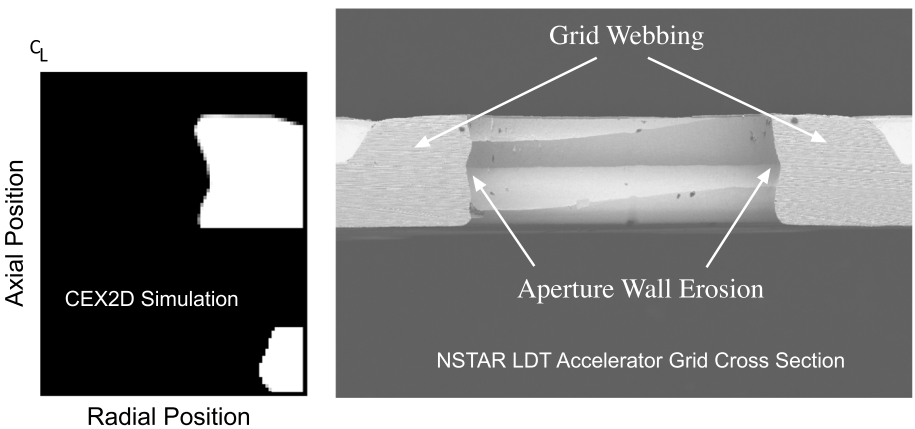

Fig. 13 Accelerator grid geometry after 8200 hours of operation predicted by CEX2D (left) and the actual erosion geometry at the center aperture revealed by cross sectioning the grid from the NSTAR LDT. The simulation accurately captures the shape of the erosion profile

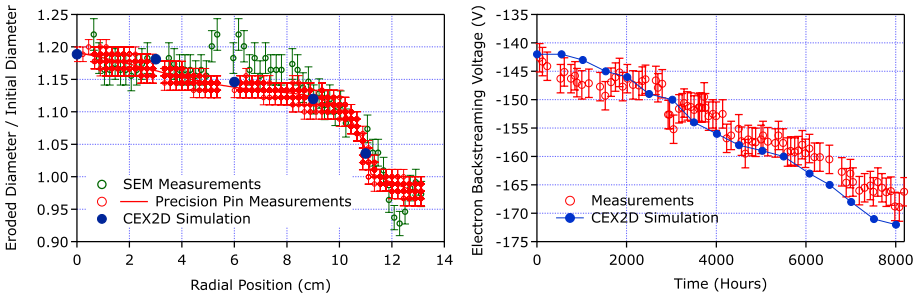

Fig. 14 Comparison of measured and calculated values of the post-test aperture diameter for the NSTAR LDT show excellent agreement (left). Predicted and measured backstreaming voltages as a function of time agree within ±5 V (right)

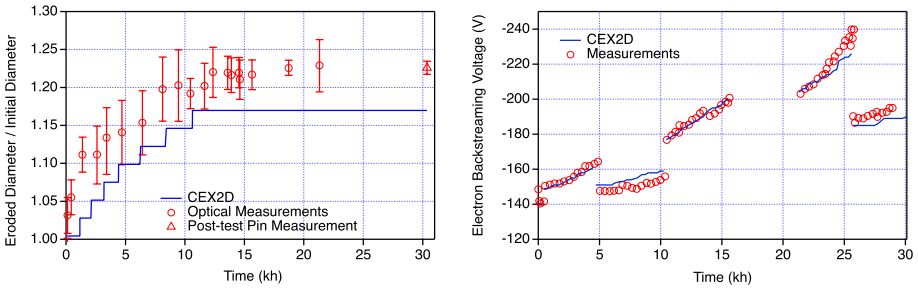

Fig. 15 Calculated center aperture erosion for the NSTAR ELT (left) is about 5% lower than measured values. Measured and predicted electron backstreaming voltages agree to within ±10–15 V (right) . The uncertainty in the electron backstreaming voltage measurements is ±2.5 V

erosion peaks in the middle of the aperture wall and that the hole edges are slightly chamfered. The hole wall erosion was simulated for five radial locations on the grid using the average upstream neutral density and sputter yields corresponding to the lower 50% likelihood curve. The final aperture diameter is compared to post-test precision pin and SEM measurements in the left plot in Fig 14. The agreement is excellent in this case, and we found that these assumptions also reproduced measurements from the NSTAR ELT, the NEXT 2000 hour test, and the NEXT LDT.

The electron backstreaming voltage measured during the NSTAR LDT is shown in the right plot in Fig. 14. As the hole diameter increases due to erosion, more negative voltage is required to prevent electron backstreaming. The hot grid gap was not known for this test, but a series of simulations run with the initial grid geometry and varying grid gaps showed that a hot gap of 0.45 mm matched the backstreaming limit measured at the beginning of the test. This gap was then held fixed in time-dependent erosion simulations that produced the erosion data in Fig. 13 and the left plot in Fig. 14. The calculated backstreaming voltages displayed in the right plot agree with the measurements to within ±5 V.

The minimum center aperture diameter measured in the NSTAR ELT [34] are compared with simulations on the left in Fig. 15. The calculated hole diameters are about 5% lower than measured values. We assumed the same initial hot grid gap of 0.45 mm, which matched the backstreaming voltage well in segment 1, as shown on the right. However, we found that 0.4 mm matched segments 2, 3, and 4 better (there are no backstreaming

data for segment 5 because it was run at the lowest power and the perveance limit was reached before backstreaming occurred). This change in hot gap is consistent with post-test measurements, which showed a change in the cold grid gap due to residual stresses in grids [34]. The backstreaming voltages calculated with the 0.4 mm grid gap agree well with measurements at the beginning of segment 6, but they diverge toward the end of that segment. This suggests that further changes in the hot grid gap occurred, although the predictions are still within about 10–15 V of the measurements. These comparisons show that CEX2D reproduces accelerator grid hole erosion quite accurately and predicts the electron backstreaming voltage for a given geometry to within about ± 15 V over a wide range of operating conditions.

The effect of backsputtered carbon on accelerator grid erosion in the next LDT

Carbon deposits on the accelerator grid in the NEXT LDT cloud the interpretation of hole erosion data. One objective of this study was to use the codes to determine whether the conditions in each test segment would lead to net erosion or net carbon deposition. These predictions were compared with images of the center aperture from each segment to help validate the models. The segments that experienced net erosion were then modeled to predict the hole wall erosion, which was compared with optical erosion measurements. CEX3D was used to model the flux, energy, and incidence angle of charge exchange ions that strike the aperture wall in order to capture any three dimensional effects. An example of the code outputs for throttle level TL37 using the beginning of test grid geometry is shown in Fig. 16. The plot in Fig. 16a displays the impingement current density as a function of axial position and azimuthal angle over the 30 degree segment modeled by CEX3D. As Fig. 2 shows, the edges of this segment are symmetry boundaries, so this pattern is repeated around the aperture. In this case the current density peaks near the downstream end of the aperture and is relatively uniform azimuthally. Figure 16b shows the mean ion energy, which peaks further upstream at about 500 eV. Ions that impact this area are formed in the interelectrode gap where the local potential is about 300 V and are then accelerated into the grid, which is at -210 V.

To determine whether these fluxes and energies are sufficient to prevent net deposition of carbon, we used a model of carbon film growth on molybdenum [49]. In steady state, a dynamic equilibrium between the rate of carbon deposition and removal by sputtering will determine the surface coverage of carbon. For sufficiently high fluxes of

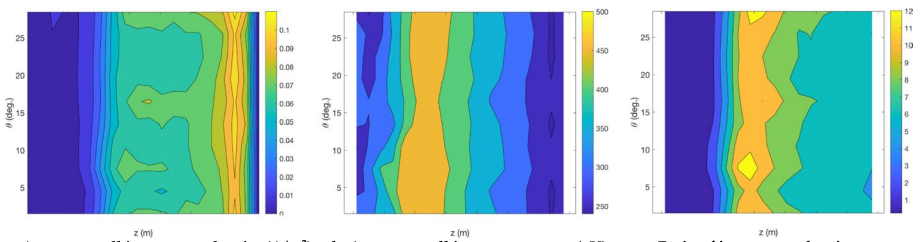

Fig. 16 Impingement current density, mean ion energy, and ratio of current density to the transition current density as a function of position on the hole wall at TL37. These are the parameters needed to determine whether the hole walls will experience net erosion or net carbon deposition

energetic xenon ions compared to the carbon backsputter rate, the equilibrium surface coverage will be negligible and will not influence the erosion rate. For ion current densities below a certain threshold at a given energy, however, multiple layers of carbon will start to form and it becomes much more difficult to remove them by sputtering. Under these conditions net deposition will occur and the underlying substrate will be protected from erosion. The threshold current density at which the transition from net erosion to net deposition occurs is given by

$$j_{\mathrm{a,trans}} = \frac{e\gamma_C S_C}{Y_C(E,\theta)} \tag{4}$$

where e is the electron charge, γ_C is the backsputtered carbon flux, S_C is the sticking coefficient for carbon on carbon (taken to be equal to unity) and Y_C is the sputter yield, dependent on energy E and angle θ, for carbon from bulk carbon [49]. To determine the transition current density we used backsputter rates measured during the NEXT LDT with a quartz crystal microbalance and the mean sputter yield based on the maximum likelihood fits to data from Yim [29]. The ratio of ion current density to the transition current density for TL37 at beginning of life is plotted in Fig. 16c. Values above one indicate that the current density and energy are high enough to prevent net deposition. In this case, most of the aperture wall will experience net erosion; only the upstream end has current densities near the transition value. Because this calculation does not depend on the sputter yield of xenon incident on molybdenum (as comparisons of predicted and

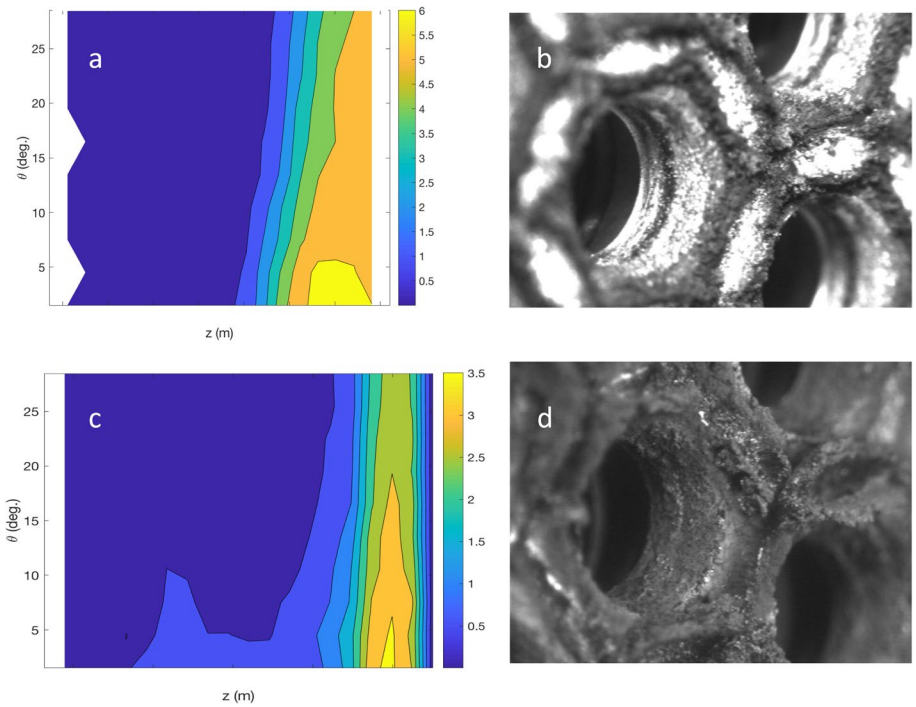

Fig. 17 (a) Predicted ratio of current density to transition current density for the NEXT LDT beginning-of-life geometry at TL40. (b) image of the center hole midway through the first segment. (c) Predicted current density ratio for TL40 with end-of-test geometry. (d) image of the center hole at the end of the test

measured erosion do), it provides an additional check of the charge exchange ion generation and trajectory models.

Calculations like these were made for the throttle levels tested in the NEXT LDT using the beginning of life grid geometry and an approximation of the end of life geometry, which incorporated larger aperture diameters and a thicker accelerator grid with dimensions based on the average of post-test measurements of the carbon deposits. An example of the analysis is shown in Fig. 17, which compares calculated current ratios and photos of the center aperture from the middle of the first segment at TL40 and the end of the test, after the last segment at TL40. At the beginning of the test the current density distribution and energies are sufficient to prevent net deposition over at least the downstream half of the aperture wall, and the photograph shows no evidence of carbon deposition in this part of the aperture. At the end of the test though, the current density distribution has shifted downstream as a result of the geometry changes and net erosion occurs only at the very end of the aperture and on the walls of the carbon deposits. This is consistent with the photograph, which shows thick deposits on the aperture walls. In these analyses we also varied the carbon sputter yield over the range of the 50% likelihood fit from Yim's analysis of sputter yield data [29] and found the same qualitative trends, so the conclusions are robust to uncertainty in this parameter.

The results of the analyses for all of the test segments are summarized in Fig. 18. The photographs of the center aperture show the evolution of the carbon deposits on the hole wall. At 6,114 hours there was still net erosion, as shown in the first photo. However, by the end of the segment the hole enlargement resulted in a reduction in charge exchange ion current density and energy and a much lower erosion rate. In addition, growth of downstream carbon deposits shifted the impingement current distribution further downstream, resulting in net erosion only at the downstream end of the aperture.

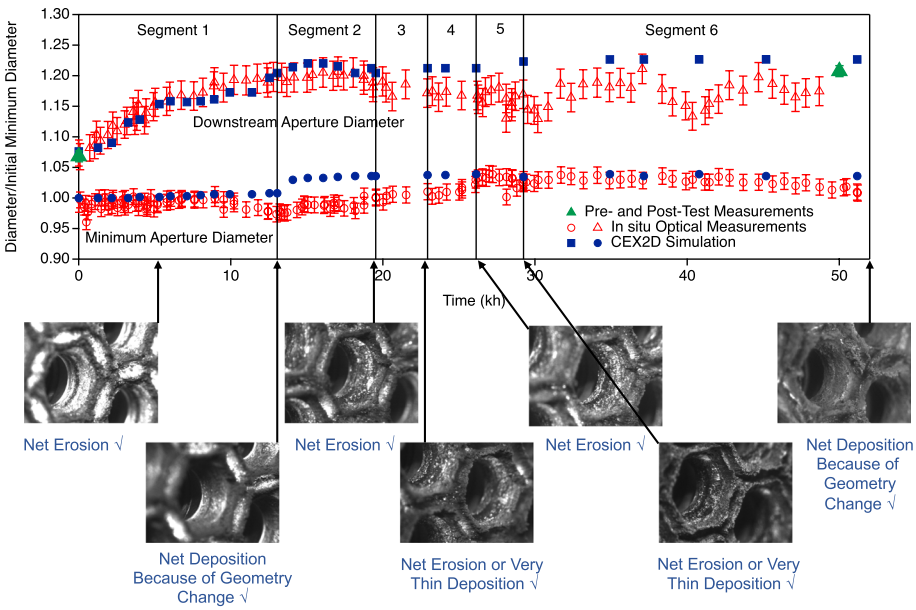

Fig. 18 Predictions of aperture diameter agree well with measurements for the NEXT LDT. The photos indicate conditions of net erosion or net deposition. Check marks indicate that the simulations agreed with the observations

This appears to be consistent with the photograph at 13,033 hours, although this conclusion is based on somewhat subjective interpretations of the light and dark zones on the photos. Interpretation of the photographs became increasing more difficult as the test progressed due to deteriorating lighting conditions and rougher surfaces.

The modeling indicates that segments 2 through 5 should have experienced net erosion at a very low rate or net deposition, although also at a low rate. The impingement current densities and energies at these throttled conditions were lower, but the carbon backsputter rates were also lower. The photographs from these test segments appear to show metal surfaces or thin carbon deposits, which is consistent with the modeling. The grid geometry in the final TL40 test segment was considerably different from the initial geometry–the holes were larger due to wall erosion and the grid was effectively thicker because of the carbon deposits on the downstream surface. As a result of these changes, the simulations show that the hole walls did not suffer significant high energy ion bombardment and experienced net deposition over most of the axial extent, as shown in Fig. 17. However, without the effective thickening of the grid due to carbon deposition and its effect on the current distribution, the aperture would have continued to erode in the final test segment.

The measured and calculated hole diameters are plotted above the photos in Fig. 18. The CEX2D code accurately captures the erosion over the first test segment and the fact that there is essentially no erosion during the next four segments due to the initial hole enlargement and the growth of carbon films on the downstream surface. The agreement between the erosion measurements and predictions and the observations of net deposition at some operating points provide further confidence in the charge exchange ion models and the erosion models.

Assessment of next life in space

After validating the codes over a range of conditions, we used them to assess the lifetime and throughput limitations for NEXT operated in space at throttle points TL1, 5, 12, 37, and 40 (shown in red in Fig. 1). These points span the throttle range and were chosen to identify the dominant failure modes at different current and voltage conditions. Screen grid failure and electron backstreaming are important in different parts of the throttling range. Screen grid erosion is not a dominant failure mode for the higher throttle levels, but appears to be the first failure mode for the lowest throttle levels. In contrast, electron backstreaming is not important for the lower levels, but is the first failure mode at the highest throttle levels. For actual applications, the codes can be used to simulate the erosion for specific throttling profiles to determine mission failure risk.

Input parameters

For these simulations the grid thicknesses, beam radius, and grid radius of curvature were based on the nominal specification, while the aperture geometries were based on pre- and post-test measurements of the grids used in the NEXT LDT. The hot grid gap was the same used in the NEXT LDT simulations, which were based on Herman's optical measurements [35]. The beam and accelerator grid voltages were set equal to the nominal throttle table values.

The discharge voltages were based on measurements from the PM1R thruster [42]. For throttle levels TL37 and TL40, these voltages were very similar to those measured in the LDT, but for the lower throttle levels the discharge voltage was 1 to 1.5 V higher than in the LDT. The discharge voltage was treated as constant in time. However, it is often observed to increase in time during wear tests, largely due to accelerator grid aperture erosion, cathode orifice erosion, and minor changes in thermal characteristics [50–52]. In the NEXT LDT the discharge voltage increased by 1 to 2 V, depending on the throttle level. These differences are unimportant for accelerator grid aperture erosion, but can have a significant impact on screen grid erosion, where the ion impact energies are close to the sputtering threshold and the yield is a steep function of energy. As shown in Fig. 19, the yield for single ions increases 23% per volt and that for double ions increases 16% per volt in the range of 23 - 28 V. The throttle levels most susceptible to screen erosion don't have much accelerator grid aperture or cathode orifice erosion, so the discharge voltage is not likely to increase much during extended operation at a low throttle level. However, missions with extended operation at high power (which experience significant hole erosion) followed by low power operation at an elevated discharge voltage may suffer greater screen grid erosion than predicted here. These cases should be investigated in more detail for particular throttling profiles.

The beamlet currents and double ion current fractions in these simulations were based on Faraday probe and ExB probe measurements, respectively, in the beam of the PM1R thruster [42]. For the upstream and downstream plasma potential and electron temperature and the neutral gas parameters we used the same values as in the NEXT LDT simulations. The ambient pressure was set to zero to simulate space conditions. For the sputter yields we used the maximum likelihood estimates from Yim's fits to data [29] for the screen grid erosion and the lower boundary of the 50% likelihood estimate for the hole wall erosion.

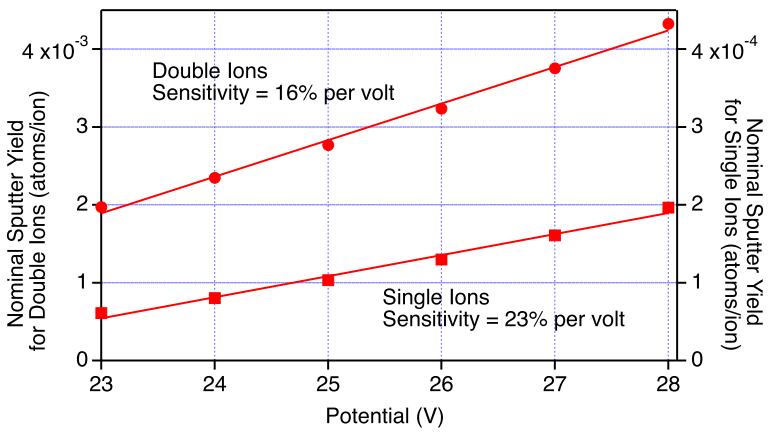

Fig. 19 Sensitivity of screen grid sputter yield to upstream plasma potential for double and single ions. Increased discharge voltage (due to cathode wear or accelerator grid aperture enlargement, for instance) can significantly increase screen grid wear rates

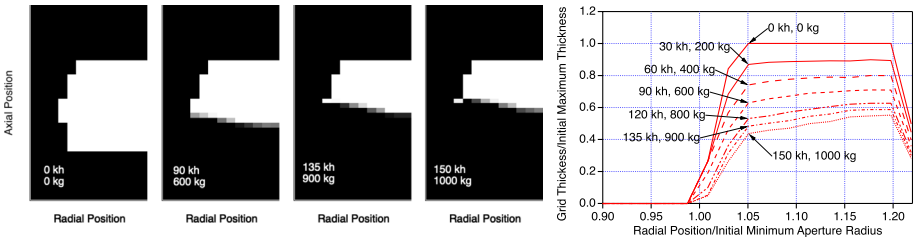

Fig. 20 Predicted screen grid erosion profiles and grid thickness as a function of time and throughput for operation in space at TL1. Approximately 50% of the grid remains after 150 kh of operation and 1000 kg of xenon throughput

Screen grid failure

At some point, thinning of the screen grid due to erosion will cause a structural failure. Prior to that, however, screen grid thinning will likely reduce the strength of the grid enough that it will deflect under the electrostatic load between the grids, resulting in a smaller grid gap. A structural analysis of the screen grid deflection due to electrostatic forces as a function of screen grid thickness shows minimal displacement down to about 25% of the original thickness, so that was used as the failure criterion. Screen grids have experienced significant erosion in wear tests without actual failure [53], so this failure criterion is likely conservative.

The predicted screen grid erosion for the lowest power level (TL1) is plotted in Fig. 20. The images on the left are the screen grid cross sections at four different times. The grid thickness as a function of time and radial position is shown on the right. About 50% of the grid remains after 150,000 hours and 1000 kg. However, it is unlikely that the thruster would be operated this long at this low power operating point. In addition, the comparisons with NSTAR and NEXT data presented above show that the model tends

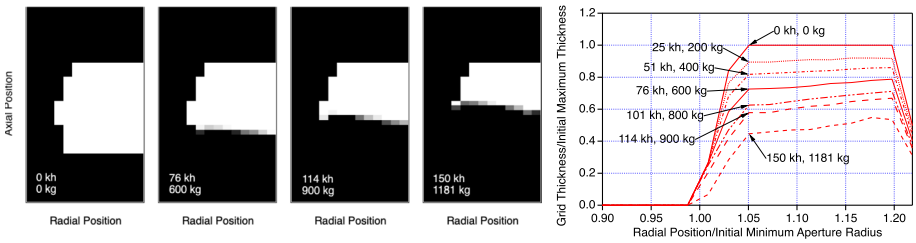

Fig. 21 Predicted screen grid erosion as a function of time and throughput for operation in space at TL12 is similar to that observed at TL1

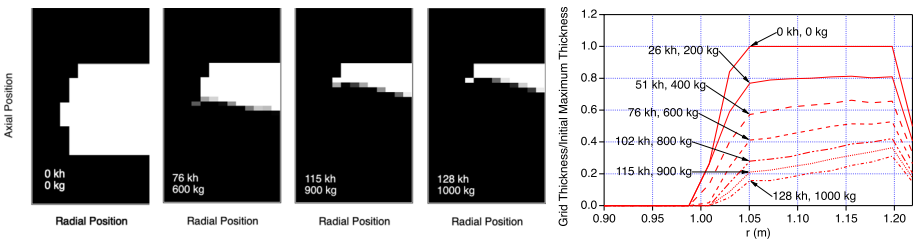

Fig. 22 Predicted screen grid erosion as a function of time and throughput for operation in space at TL5, where it is the dominant failure mode

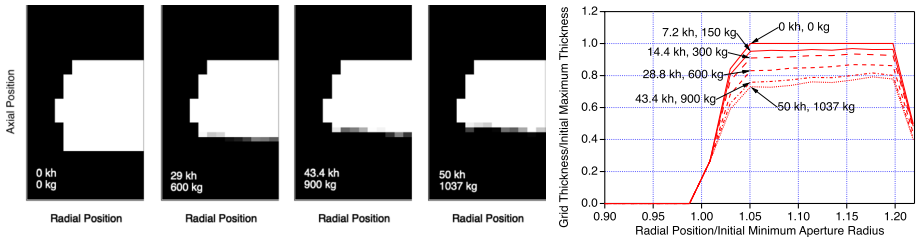

Fig. 23 Predicted screen grid erosion as a function of time and throughput for operation in space at TL40. For the higher power levels, screen grid erosion rates are relatively low and electron backstreaming is the dominant failure mode

to overestimate the screen erosion, so these results are likely conservative. The results for TL12, plotted in Fig. 21, are similar.

The worst case condition is TL5. The results for this low power condition plotted in Fig. 22 show that it reaches a thickness of 25% after about 122,000 hours, after processing 900 kg of xenon. In this case, low voltage operation leads to poor transparency, as shown in Fig. 9. Even though the beam current is over three times lower, the screen grid current is nearly as high as at full power. The rate at which propellant is processed is proportional to the beam current, so at this operating point the amount of screen grid erosion experienced per kg of propellant consumed is much larger. This is exacerbated by the fact that the discharge voltage at TL5 is about three volts higher than at TL40.

The screen erosion for operation at the peak power (TL40) is shown in Fig. 23. Even after 50,000 hours of operation, in which over 1000 kg of propellant is consumed, the

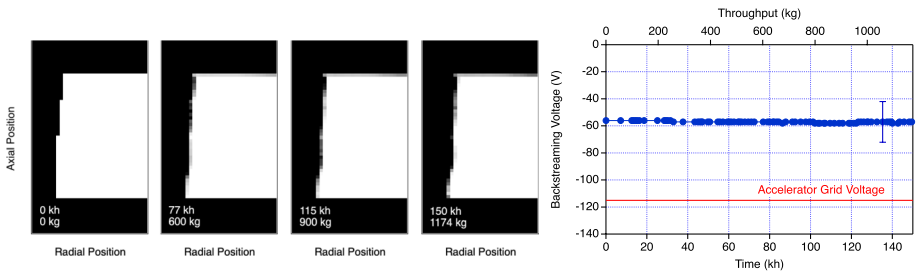

Fig. 24 Predicted accelerator grid erosion profiles and backstreaming voltage for operation in space at TL5 show that failure due to backstreaming is not a significant risk. The error bar represents the ±15 V uncertainty in the predicted backstreaming voltage

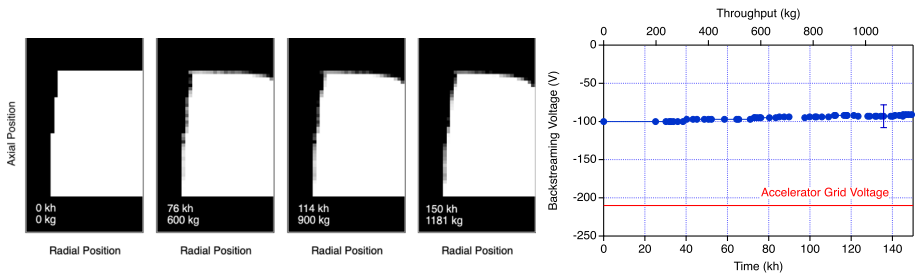

Fig. 25 Predicted accelerator grid aperture erosion for operation in space at TL12 is low and electron backstreaming voltage is essentially constant

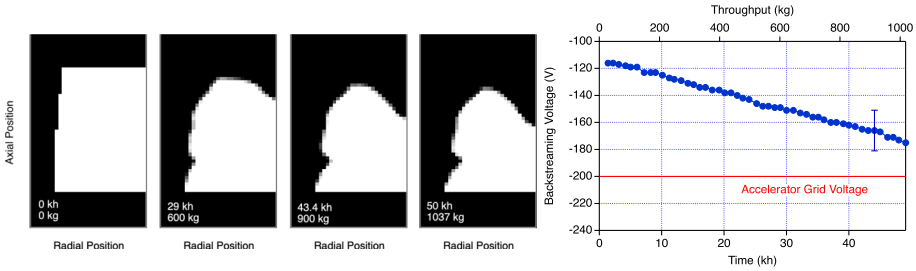

Fig. 26 Predicted accelerator grid erosion for operation in space at TL37 is significant and backstreaming voltage margin decreases. At 50 kh and 1000 kg throughput, however, there is still margin even considering ±15 V uncertainty in the predicted values

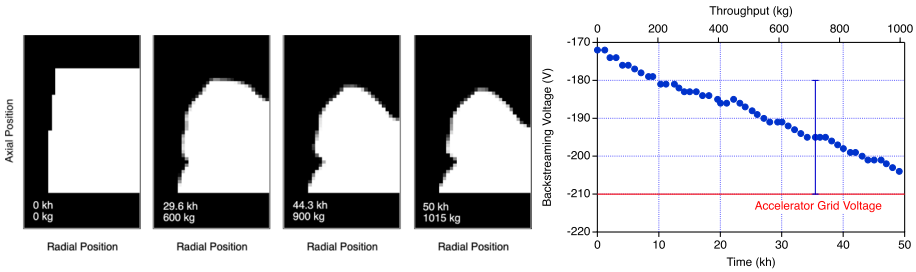

Fig. 27 Predicted erosion and backstreaming voltage as a function of time and throughput at TL40. With the ±15 V model uncertainty, failure could occur after about 35 kh and 700 kg of throughput

grid has lost only about 25% of its original thickness. In this case, screen erosion is not the dominant failure mode. The results for TL37 are similar to those for TL40.

Electron backstreaming

Failure in this case is taken to be the point at which the nominal accelerator grid voltage can no longer prevent electron backstreaming for the eroded geometry. Accelerator grid erosion profiles and electron backstreaming voltage as a function of time and throughput compared to the nominal grid voltage are shown in Figs. 24 and 25 for throttle levels 5 and 12. The low throttle levels exhibit very low erosion rates, so electron backstreaming is not a credible failure mode.

Figure 26 shows the accelerator grid cross sections at several times and the resulting change in the electron backstreaming voltage as a function of time at TL37. The model predicts minimal erosion of the upstream hole edge, the formation of a notch in the hole wall due to charge exchange ion focusing into that region, and chamfering of the downstream hole edge. CEX2D does not accurately model the inherently three-dimensional pits and grooves erosion pattern that forms on the downstream surface, so the downstream features should be ignored. The nominal accelerator grid voltage at TL37 is -200 V, so even after 50,000 hours and more than 1000 kg of xenon throughput, the accelerator grid still has about 25 V margin. Even with the uncertainty of ±15 V in predicted voltages compared to measurements that was found in comparisons with NSTAR and NEXT ground test data, the engine should not experience failure due to backstreaming in this period.

The predicted erosion profiles and change in the backstreaming limit over time for TL40 are shown in Fig. 27. In this case, the nominal accelerator grid voltage is -210 V, so the model predicts failure after greater than 50,000 hours and over 1000 kg of xenon throughput. However, with the ±15 V model uncertainty, failure could occur at as low as 700 kg throughput. The thruster life could be extended by increasing the magnitude of the accelerator grid voltage at some point during the mission to provide more margin against backstreaming. This comes at the expense of increased erosion rates, but significant gains in throughput can be achieved with modest changes in accelerator grid voltage.

Summary and conclusions

The ion optics erosion codes CEX2D and CEX3D were employed to assess the lifetime limits of NEXT in space due to screen grid and accelerator grid aperture erosion over a range of operating conditions that span the throttle table. The code inputs for the deterministic analysis were nominal values based primarily on measurements from high fidelity hardware that are representative of what would be expected in flight operation. The input parameters with the greatest uncertainty are the neutral density distribution upstream of the grids, which is a primary driver of charge exchange ion formation and strongly influences accelerator grid erosion, the sputter yield variation with energy and incidence angle, which affects erosion of both grids, and the hot grid gap, which influences the ion focusing. The neutral density was assumed to be uniform and equal to an average value that is consistent with the total neutral flow from the engine. The sputter yield in the range of energies relevant for accelerator grid erosion was assumed to be at the low end of experimental measurements. For screen grid sputtering at energies near threshold we assumed the nominal yield based on sparse measurements in this energy range. Measurements of the hot grid gap in NEXT were used for those simulations, but in some validation cases we had to infer the grid gap by matching electron backstreaming voltage at beginning of life or downstream accelerator grid erosion patterns. As noted in Input Parameters for the Validation Cases section, measured backstreaming voltage is a sensitive indicator of grid gap. These choices represent our current best estimates of the nominal input parameter values and led to good agreement with measured accelerator grid erosion and conservative values of screen grid erosion for two different thrusters and a wide range of operating conditions.

The screen grid erosion models were validated by measurements of screen grid transparency and grid erosion rates in wear tests of NSTAR engines and NEXT. Comparisons of measured and calculated screen grid current showed good agreement, demonstrating that the models of the primary ion impingement are accurate. However, the calculated values of screen grid erosion were generally two to three times higher than measured values, suggesting that the actual sputter yield near threshold is lower than current data and semi-empirical curve fits would suggest. The accelerator grid erosion models were validated with measurements of electron

backstreaming voltage and aperture enlargement in NSTAR and NEXT wear tests. The calculated electron backstreaming voltage for well-characterized beginning of life grid geometries agreed with measurements to within ± 15 V and the difference was correlated with the perveance fraction, suggesting some model error in the charge density or potential calculation. The agreement between measured and calculated grid erosion and backstreaming voltage as a function of time was excellent for both NSTAR and NEXT.

The codes were also used to assess the impact that accelerator grid carbon deposits had on the aperture erosion rates in the NEXT LDT. Using a model that predicts the current density at which the transition between net erosion and net deposition occurs, we predicted the conditions under which carbon should accumulate on the aperture walls. These predictions agreed well with observations, providing another demonstration that the models accurately reproduce the flux and energy of charge exchange ions striking the hole walls. Combining these results with predictions of aperture erosion, we concluded that the carbon deposits prevented erosion that otherwise would have occurred in the final test segment at full power. However, the calculated erosion agreed well with the observed aperture enlargement from the first segment, which experienced net carbon deposition only at the very end. The subsequent low power operating points from the throttle profile test suffered little or no carbon deposition, but were not subject to significant aperture erosion anyway. Although the wear characteristics of some portions of the NEXT LDT were not representative of operation in space due to carbon backsputtering, it still provided a wealth of data that helped validate the erosion models.

The validated codes were then used to predict the time to failure in space due to screen grid failure or electron backstreaming. We found that screen grid erosion was only important at low throttle levels, leading to failure after processing 900 kg of propellant at TL5, or over 1000 kg at TL1 and 12. As noted above, the code tends to overpredict screen grid erosion rates by a factor of two to three, so these results are likely quite conservative. In addition, it is unlikely that this amount of propellant would be processed at these low throttle levels. This erosion could also be mitigated to a large extent by operating at conditions with better transparency and at flow rates that reduce the discharge voltage by a volt or two.

Accelerator grid erosion ultimately leading to electron backstreaming was found to be the dominant failure mode at high power levels. Electron backstreaming would occur after processing more than 1000 kg of xenon at TL37 and after about 700 kg for TL40, even with margin added to accommodate the ± 15 V error in calculated backstreaming voltage. The simulations of accelerator grid structural failure due to erosion in the pits and grooves pattern on the downstream grid face [5] yielded predicted time to failure that was greater than that for electron backstreaming. These simulations were more difficult to validate, but generally predicted higher erosion rates than those observed, so these results are likely conservative. Therefore, backstreaming due to hole wall erosion is the first failure mechanism. If necessary, electron backstreaming at a given operating point could be delayed by increasing the accelerator grid voltage during the mission.

Table 2 Sources of data used to define CEX2D and CEX3D code input parameters

Parameter	NSTAR 8200 Hour LDT	NSTAR 30,352 Hour ELT	NEXT 2000 Hour Test	NEXT 51,184 Hour LDT	NEXT Space Conditions
Geometry					
Screen Grid Thickness	Post-test SEM measurements [41]	Specification, corrected for stretching during dishing [34]	Specification	Pre-test measurements at edge, post-test SEM measurements corrected for erosion and thinning due to dishing	Specification
Accelerator Grid Thickness	Post-test SEM measurements [41]	Specification	Specification	Post-test SEM measurements	Specification
Screen Aperture Geometry	Post-test measurements [41]	Specification (minimum hole diameter), post-test SEM measurements (upstream and downstream diameters) [34]	Pre-test pin measurements (minimum hole diam), post-test measurements (upstream and downstream diameters)	Pre-test pin measurements (minimum hole diam), post-test measurements (upstream and downstream diameters)	Specification (minimum hole diam), NEXT LDT post-test measurements (upstream and downstream diameters)
Accelerator Aperture Geometry	Specification (minimum hole diameter), post-test measurements (upstream and downstream diameters) [41]	Pre-test pin measurements (minimum hole diam), post-test SEM measurements (upstream and downstream diameters) [34]	Pre-test pin measurements (minimum hole diam), post-test measurements (upstream and downstream diameters)	Pre-test pin and putty measurements	Specification (minimum hole diam), NEXT LDT pre-test measurements (upstream and downstream diameters)
Grid Gap	Inferred from BOL electron backstreaming simulations	Assumed to be the same as the NSTAR LDT grids	Inferred from characteristics of erosion pattern	Optical measurements of hot grid gap [35]	Optical measurements of hot grid gap [35]
Optics Radius of Curvature	Specification	Specification	Specification	Specification	Specification
Beam Radius	Specification	Specification	Specification	Specification	Specification
Electrical Parameters					
Beam Voltage	Nominal voltage from throttle table [41]	Nominal voltage from throttle table [37]	Nominal voltage from throttle table [38]	Nominal voltage from throttle table [14]	Nominal voltage from throttle table [14]
Discharge Voltage	Average values from each segment measured at the thruster [41]	Average values from each segment measured at the thruster [37]	BOL values measured at the thruster [38]	BOL values measured at the thruster [14]	Measurements on PM1R thruster [42]
Accelerator Grid Voltage	Nominal voltage from throttle table [41]	Nominal voltage from throttle table [37]	Nominal voltage from throttle table [38]	Nominal voltage from throttle table [14]	Nominal voltage from throttle table [14]
Upstream Plasma Properties					
Beamlet Current	Faraday probe measurements, extrapolated back to grid [36]	Faraday probe measurements, extrapolated back to grid [15, 36, 37]	Faraday probe measurements, extrapolated back to grid [38]	Measurements at 3.52 and 1.2 A extrapolated to grid; 1.0 A scaled from 1.2 A data [14]	Faraday probe measurements on PM1R thruster [42]
Plasma Density	Determined iteratively from jb in CEX2D; these values then used in CEX3D	Determined iteratively from jb in CEX2D; these values then used in CEX3D	Determined iteratively from jb in CEX2D; these values then used in CEX3D	Determined iteratively from jb in CEX2D; these values then used in CEX3D	Determined iteratively from jb in CEX2D; these values then used in CEX3D

Table 2 (continued)

Parameter	NSTAR 8200 Hour LDT	NSTAR 30,352 Hour ELT	NEXT 2000 Hour Test	NEXT 51,184 Hour LDT	NEXT Space Conditions
Plasma Potential	Assumed equal to discharge voltage (consistent with emissive probe measurements on LM thruster) [39]	Assumed equal to discharge voltage (consistent with emissive probe measurements on LM thruster) [39]	Assumed equal to discharge voltage (consistent with emissive probe measurements on LM thruster) [40]	Assumed equal to discharge voltage (consistent with emissive probe measurements on LM thruster) [40]	Assumed equal to discharge voltage (consistent with emissive probe measurements on LM thruster) [40]
Electron Temperature	5 eV for all cases (consistent with Langmuir probe measurements on LM thruster) [39]	5 eV for all cases (consistent with Langmuir probe measurements on LM thruster) [39]	5 eV for all cases (consistent with Langmuir probe measurements on LM thruster) [40]	5 eV for all cases (consistent with Langmuir probe measurements on LM thruster) [40]	5 eV for all cases (consistent with Langmuir probe measurements on LM thruster) [40]
Double Ion Current Fraction	ExB probe measurements in LDT and on LM thruster [15, 41]	ExB probe measurements of centerline values [15, 41]	ExB probe measurements on EM thruster [42]	ExB probe measurements on EM thruster [42]	ExB probe measurements on PM1R thruster [42]
Downstream Plasma Properties					
Plasma Potential	Emissive probe measurements of 3-5 V from NSTAR LDT and an average measured value for Vg of about 10V [36, 41]	Emissive probe measurements of 3-5 V from NSTAR LDT and an average measured value for Vg of about 10V [36, 41]	Emissive probe measurements of 3V from LM thruster [43] and an average measured value for Vg of about 10V from 2000 hour test	Emissive probe measurements of 3V from LM thruster [43] and an average measured value for Vg of about 10V from NEXT LDT	Emissive probe measurements of 3V from LM thruster [43] and an average measured value for Vg of about 10V from NEXT LDT
Electron Temperature	Measurements from DS1 [44]	Measurements from DS1 [44]	2 eV; assumed to be similar to NSTAR	2 eV; assumed to be similar to NSTAR	2 eV; assumed to be similar to NSTAR
Neutral Gas Properties					
Upstream Neutral Density	Average value, calculated from measured beam current, propellant efficiency, accelerator grid open area fraction, and chamber temperature [46]	Average value, calculated from measured beam current, propellant efficiency, accelerator grid open area fraction, and chamber temperature [46]	Average value, calculated from measured beam current, propellant efficiency, accelerator grid open area fraction, and chamber temperature [47]	Average value, calculated from measured beam current, propellant efficiency, accelerator grid open area fraction, and chamber temperature [47]	Average value, calculated from measured beam current, propellant efficiency, accelerator grid open area fraction, and chamber temperature [47]
Vacuum Chamber Pressure	Measured value, gauge calibrated on Xe [41]	Measured value, gauge calibrated on Xe [37]	Measured value, gauge calibrated on N2, corrected for Xe [38]	Measured value, gauge calibrated on N2, corrected for Xe using scale factor of 2.5	N/A
Upstream Gas Temperature	Based on discharge chamber temperatures measured in EM thruster [46]	Based on discharge chamber temperatures measured in EM thruster [46]	Based on discharge chamber temperatures measured in PM1 thruster [47]	Based on discharge chamber temperatures measured in PM1 thruster [47]	Based on discharge chamber temperatures measured in PM1 thruster [47]
Accelerator Grid Temperature	Based on accelerator grid stiffener temperatures measured in NSTAR EM thruster [46]	Based on accelerator grid stiffener temperatures measured in NSTAR EM thruster [46]	Based on accelerator grid stiffener temperatures measured in PM1 thruster [47]	Based on discharge chamber temperatures measured in PM1 thruster [47]	Based on discharge chamber temperatures measured in PM1 thruster [47]
Downstream Gas Temperature	Chamber wall temperature	Chamber wall temperature	Chamber wall temperature	Chamber wall temperature	N/A

Appendix A Sources of data for model inputs

The codes require the parameters listed in the first column of Table 2 as inputs. These are organized under the categories of optics geometry, the potentials applied to the thruster components, plasma properties in the discharge chamber and the beam, and the neutral gas properties. The sources of data used to define these parameters for each of the tests used in model validation are summarized in the table.

Authors' contributions
All authors contributed to the research. Simulations were conducted by James Polk and Vernon Chaplin. Modifications to the codes as part of this work were done by Vernon Chaplin with contributions from James Polk. John Anderson provided the DAC neutral simulations. Other coauthors provided input and validation data, reviewed the results, and offered valuable insights and suggestions. The authors read and approved the final manuscript.

Funding
The research described in this paper was carried out in part at the Jet Propulsion Laboratory, California Institute of Technology, under a contract with the National Aeronautics and Space Administration.

Availability of data and materials
Data are available upon reasonable request to the authors.

Code availability
The CEX2D and CEX3D codes may be licensed from the Jet Propulsion Laboratory, California Institute of Technology, subject to ITAR restrictions.

Declarations

Competing interests
The authors declare that they have no known competing financial interests or personal relationships that could have influenced the work reported in this paper.

Received: 3 April 2022 Accepted: 5 March 2023
Published online: 12 April 2023

References

1. Herman DA (2009) NEXT Long-Duration Test Neutralizer Performance and Erosion Characteristics. Paper IEPC-2009-154, presented at the 31st International Electric Propulsion Conference, Ann Arbor, Michigan, 20–24 September, 2009
2. Shastry R, Soulas G, Aulisio M, Schmidt G (2017) Current Status of NASA's NEXT-C Ion Propulsion System Development Project. Paper IAC-17.C4.4.3, presented at the 68th International Astronautical Congress, Adelaide, Australia, 25–29 September 2017. https://ntrs.nasa.gov/citations/20180001491
3. Brophy J, Polk J, Randolph T (2008) Lifetime Qualification Standards for Electric Thrusters for Deep-Space Missions. Paper AIAA-2008-5184, presented at the 44th AIAA/ASME/SAE/ASEE Joint Propulsion Conference, Hartford, Connecticut, 21–23 July, 2008. https://doi.org/10.2514/6.2008-5184
4. Dankanich JW, Brophy JR, Polk JE (2009) Lifetime Qualification Standard for Electric Thrusters. Paper AIAA 2009-5095, presented at the 45th AIAA/ASME/SAE/ASEE Joint Propulsion Conference, Denver, Colorado, 2–5 August, 2009. https://doi.org/10.2514/6.2009-5095
5. Chaplin VH, Polk JE, Katz I, Anderson JR, Williams GJ, Soulas GC, Yim JT (2018) 3d simulations of ion thruster accelerator grid erosion accounting for charge exchange ion space charge. Paper AIAA-2018-4812 presented at the 54th AIAA/ASME/SAE/ASEE Joint Propulsion Conference, Cincinnati, Ohio, 9–11 July, 2018. https://doi.org/10.2514/6.2018-4812
6. Yim JT, Williams GJ, Shastry GCR, Soulas, Chaplin VH, Polk JE (2019) Uncertainty Quantification of Modeled Electron Backstreaming Failure for the NEXT Ion Thruster. Paper IEPC-2019-722, presented at the 36th International Electric Propulsion Conference, University of Vienna, Austria, 15–20 September, 2019
7. Patterson MJ, Benson SW (2007) NEXT Ion Propulsion System Development Status and Performance. Paper AIAA-2007-5199, presented at the 43rd AIAA/ASME/SAE/ASEE Joint Propulsion Conference, Cincinnati, Ohio, 8–11 July, 2007. https://doi.org/10.2514/6.2007-5199
8. Soulas GC, Patterson MJ (2007) NEXT Ion Thruster Performance Dispersion Analyses. Paper AIAA-2007-5213, presented at the 43rd AIAA/ASME/SAE/ASEE Joint Propulsion Conference, Cincinnati, Ohio, 8–11 July, 2007. https://doi.org/10.2514/6.2007-5213
9. Frandina MM, Arrington LA, Soulas GC, Hickman TA, Patterson MJ (2005) Status of the NEXT Ion Thruster Long Duration Test. Paper AIAA-2005-4065, presented at the 41st AIAA/ASME/SAE/ASEE Joint Propulsion Conference, Tucson, Arizona, 10–13 July, 2005. https://doi.org/10.2514/6.2005-4065
10. Herman DA, Soulas GC, Patterson MJ (2008) Performance Characteristics of the NEXT Long-Duration Test after 16,550 h and 337 kg of Xenon Processed. Paper AIAA-2008-4527, presented at the 44th AIAA/ASME/SAE/ASEE Joint Propulsion Conference, Hartford, Connecticut, 21–23 July, 2008. https://doi.org/10.2514/6.2008-4527

11. Patterson MJ, Foster JE, Haag TW, Rawlin VK, Soulas GC, Roman RF (2002) NEXT: NASA's Evolutionary Xenon Thruster. Paper AIAA-2002-3832, presented at the 38th AIAA/ASME/SAE/ASEE Joint Propulsion Conference, Indianapolis, Indiana, 7–10 July, 2002. https://doi.org/10.2514/6.2002-3832
12. Soulas GC, Domonkos MT, Patterson MJ (2003) Performance Evaluation of the NEXT Ion Engine. Paper AIAA-2003-5278, presented at the 39th AIAA/ASME/SAE/ASEE Joint Propulsion Conference, Huntsville, Alabama, 20–23 July, 2003. https://doi.org/10.2514/6.2003-5278
13. Herman DA (2010) Status of the NASA's Evolutionary Xenon Thruster (NEXT) Long-Duration Test after 30,352 Hours of Operation. Paper AIAA-2010-7112, presented at the 46th AIAA/ASME/SAE/ASEE Joint Propulsion Conference, Nashville, Tennessee, 25–28 July, 2010. https://doi.org/10.2514/6.2010-7112
14. Shastry R, Herman DA, Soulas GC, Patterson MJ (2014) End-of-test Performance and Wear Characterization of NASA's Evolutionary Xenon Thruster (NEXT) Long-Duration Test. Paper AIAA 2014-3617, presented at the 50th AIAA/ASME/SAE/ASEE Joint Propulsion Conference, Cleveland, Ohio, 28–30 July, 2014. https://doi.org/10.2514/6.2014-3617
15. Wirz RE, Katz I, Goebel DM, Anderson JR (2011) Electron Backstreaming Determination for Ion Thrusters. J Propuls Power 27(1):206–210. https://doi.org/10.2514/1.46844
16. Wirz RE, Anderson JR, Katz I (2011) Time-Dependent Erosion of Ion Optics. J Propuls Power 27(1):211–217. https://doi.org/10.2514/1.46845
17. Anderson JR, Katz I, Goebel DM (2004) Numerical Simulation of Two-Grid Ion Optics Using a 3D Code. Paper AIAA-2004-3782, presented at the 40th AIAA/ASME/SAE/ASEE Joint Propulsion Conference, Ft. Lauderdale, Florida, 11–14 July, 2004. https://doi.org/10.2514/6.2004-3782
18. Nakano M (2008) Three-dimensional simulations of grid erosion in ion engines. Vacuum 83(1):82–85. https://doi.org/10.1016/j.vacuum.2008.03.080
19. Shagayda A, Nikitin V, Tomilin D (2016) Three-dimensional analysis of ion optics with misalignments of apertures. Vacuum 123:140–150. https://doi.org/10.1016/j.vacuum.2015.10.030
20. Mikellides IG, Jongeward GA, Katz I, Manzella DH (2002) Plume Modeling of Stationary Plasma Thrusters and Interactions with the Express-A Spacecraft. J Spacecr Rocket 39(6):894–903. https://doi.org/10.2514/2.3896
21. Herman DA, Soulas GC, Patterson MJ (2008) NEXT Long-Duration Test Plume and Wear Characteristics after 16,550 h and 337 kg of Xenon Processed. Paper AIAA-2008-4919, presented at the 44th AIAA/ASME/SAE/ASEE Joint Propulsion Conference, Hartford, Connecticut, 21–23 July, 2008. https://doi.org/10.2514/6.2008-4919
22. Miller JS, Pullins SH, Levandier DJ, Chiu Y, Dressler RA (2002) Xenon charge exchange cross sections for electrostatic thruster models. J Appl Phys 91(3):984–991. https://doi.org/10.1063/1.1426246
23. Birdsall CK, Langdon AB (2004) Plasma Physics Via Computer Simulation. Series in Plasma Physics, Taylor and Francis, Boca Raton
24. Araki SJ, Wirz RE (2013) Ion-neutral collision modeling using classical scattering with spin-orbit free interaction potential. IEEE Trans Plasma Sci 41(3):470–480. https://doi.org/10.1109/TPS.2013.2241457
25. Araki SJ, Wirz RE (2015) Modeling of Elastic Collisions between High Energy Ions and Slow Neutral Atoms. Paper IEPC-2015-202, presented at the 34th International Electric Propulsion Conference, Hyogo-Kobe, Japan 4–10 July, 2015
26. Patino MI, Wirz RE (2018) Characterization of Xenon Ion and Neutral Interactions in a Well-Characterized Experiment. Phys. Plasmas 25:062108. https://doi.org/10.1063/1.5030464
27. Eckstein W (2003) New Fit Formulae for the Sputtering Yield. J Nucl Mater 329:209–213. https://doi.org/10.1016/S0022-3115(03)00192-2
28. Wei Q, Li K, Lian J, Wang L (2008) Angular Dependence of Sputtering Yield of Amorphous and Polycrystalline Materials. J Phys D Appl Phys 41:172002. https://doi.org/10.1088/0022-3727/41/17/172002
29. Yim JT (2017) A survey of xenon ion sputter yield data and fits relevant to electric propulsion spacecraft integration. Paper IEPC-2017-060, presented at the 35th International Electric Propulsion Conference, Georgia Institute of Technology, Atlanta, Georgia, 8–12 October, 2017
30. Farnell CC (2007) Performance and Lifetime Simulation of Ion Thruster Optics. Colorado State University, PhD
31. Yalin AP, Williams JD, Surla V, Zoerb KA (2011) Differential sputter yield profiles of molybdenum due to bombardment by low energy xenon ions at normal and oblique incidence. J Phys D Appl Phys 40:3194–3202. https://doi.org/10.1088/0022-3727/40/10/025
32. Oyarzabal E, Yu JH, Doerner RP, Tynan GR, Schmid K (2006) Molybdenum angular sputtering distribution under low energy xenon ion bombardment. J Appl Phys 100(6):063301. https://doi.org/10.1063/1.2336502
33. Diaz EM, Soulas GC (2005) Grid Gap Measurement for an NSTAR Ion Thruster. Paper IEPC–2005–244 presented at the 29th International Electric Propulsion Conference, Princeton University, Princeton, New Jersey, 31 October–4 November, 2005
34. Anderson JR, Sengupta A, Brophy JR (2004) Post-Test Analysis of the Deep Space One Spare Flight Thruster Ion Optics. Paper AIAA-2004-3010, presented at the 40th AIAA/ASME/SAE/ASEE Joint Propulsion Conference, Ft. Lauderdale, Florida, 11–14 July, 2004. https://doi.org/10.2514/6.2004-3010
35. Herman DA, Patterson MJ, Soulas GC (2008) NASA's Evolutionary Xenon Thruster (NEXT) Prototype-Model Ion Optics Operating Grid-Gap Measurements. Paper presented at the 68th JANNAF Propulsion Meeting, Orlando, Florida, 8–12 December, 2008. https://www.jannaf.org/howtoorder
36. Brophy JR (2007) Propellant Throughput Capability of the Dawn Ion Thrusters. Paper IEPC-2007-279, presented at the 30th International Electric Propulsion Conference, Florence, Italy, 17–20 September, 2007
37. Sengupta A, Brophy JR, Goodfellow KD (2003) Status of the Extended Life Test of the Deep Space 1 Flight Spare Ion Engine After 30,352 Hours of Operation. Paper AIAA-2003-4558, presented at the 39th AIAA/ASME/SAE/ASEE Joint Propulsion Conference, Huntsville, Alabama, 20–23 July, 2003. https://doi.org/10.2514/6.2003-4558
38. Kamhawi H, Soulas G, Patterson M, Frandina M (2004) NEXT Ion Engine 2000 Hour Wear Test Plume and Erosion Results. Paper AIAA-2004-3791, presented at the 40th AIAA/ASME/SAE/ASEE Joint Propulsion Conference, Ft. Lauderdale, Florida, 11–14 July, 2004. https://doi.org/10.2514/6.2004-3791
39. Sengupta A, Goebel DM, Owens AG (2009) Langmuir Probe Studies of Magnetic Confinement in an Ion Thruster Discharge Plasma. J Propul Power 25(2):387–396. https://doi.org/10.2514/1.36547

40. Herman DA (2005) The Use of Electrostatic Probes to Characterize the Discharge Plasma Structure and Identify Discharge Cathode Erosion Mechanisms in Ring-Cusp Ion Thrusters. University of Michigan, PhD
41. Polk JE, Anderson JR, Brophy JR, Rawlin VK, Patterson MJ, Sovey J, Hamley J (1999) An Overview of the Results from an 8200 Hour Wear Test of the NSTAR Ion Thruster. Paper AIAA 99-2446, presented at the 35th AIAA/ASME/SAE/ASEE Joint Propulsion Conference, Los Angeles, California, 20–24 June, 1999. https://doi.org/10.2514/6.1999-2446
42. Pollard JE, Diamant KD, Crofton MW, Patterson MJ, Soulas GC (2010) Spatially-Resolved Beam Current and Charge-State Distributions for the NEXT ion Engine. Paper AIAA 2010-6779, presented at the 46th AIAA/ASME/SAE/ASEE Joint Propulsion Conference, Nashville, Tennessee, 25–28 July, 2010. https://doi.org/10.2514/6.2010-6779
43. Foster JE, Patterson MJ, Pencil E, McEwen H, Diaz E (2006) Plasma Characteristics Measured in the Plume of a NEXT Multi-Thruster Array. Paper AIAA 2006-5181, presented at the 42nd AIAA/ASME/SAE/ASEE Joint Propulsion Conference, Sacramento, California, 9–12 July, 2006. https://doi.org/10.2514/6.2006-5181
44. Brinza D, Mactutis AT, McCarty KP, Rademacher JD, van Zandt TR, Narvaez P, Wang JJ, Tsurutani BT, Katz I, Davis VA, Moses S, Musmann G, Kuhnke F, Richter I, Othmer C, Glassmeier KH, Henty MD (2001) Plasma Characteristics Measured in the Plume of a NEXT Multi-Thruster Array. Paper AIAA 2001-0966, presented at the 39th AIAA Aerospace Sciences Meeting, Reno, Nevada, 8–11 January, 2001. https://doi.org/10.2514/6.2001-966
45. Sengupta A, Goebel D, Fitzgerald D, Owens A, Tynan G, Doerner R (2004) Experimentally Determined Neutral Density and Plasma Parameters in a 30cm Ion Engine. Paper AIAA-2004-3613, presented at the 40th AIAA/ASME/SAE/ASEE Joint Propulsion Conference, Ft. Lauderdale, Florida, 11–14 July, 2004. https://doi.org/10.2514/6.2004-3613
46. Rawlin VK, Patterson MJ, Becker RA (1997) Thermal Environmental Testing of NSTAR Engineering Model Ion Thrusters. Paper IEPC-97-051, presented at the 25th International Electric Propulsion Conference, Cleveland, Ohio, 24–28 August, 1997
47. Anderson JR, Snyder JS, Van Noord JL, Soulas GC (2007) Thermal Development Test of the NEXT PM1 Ion Engine. Paper AIAA-2007-5217, presented at the 43rd AIAA/ASME/SAE/ASEE Joint Propulsion Conference, Cincinnati, Ohio, 8–11 July, 2007. https://doi.org/10.2514/6.2007-5217
48. LeBeau GJ, Lumpkin FE (2001) Application highlights of the DSMC analysis code (DAC) software for simulating rarefied flows. Comput Methods Appl Mech Eng 191(6–7):595–609. https://doi.org/10.1016/S0045-7825(01)00304-8
49. Soulas GC (2013) The Impact of Back-Sputtered Carbon on the Accelerator Grid Wear Rates of the NEXT and NSTAR Ion Thrusters. Paper IEPC-2013-157, presented at the 33rd International Electric Propulsion Conference, The George Washington University, Washington, D.C., 6–10 October, 2013
50. Polk JE, Anderson JR, Brophy JR, Rawlin VK, Patterson MJ, Sovey JS (1997) The Effect of Engine Wear on Performance in the NSTAR 8000 Hour Ion Engine Endurance Test. Paper AIAA-97-3387, presented at the 33rd AIAA/ASME/SAE/ASEE Joint Propulsion Conference, Seattle, Washington, 6–9 July, 1997. https://doi.org/10.2514/6.1997-3387
51. Goebel DG, Polk JE, Mikellides IG (2011) Ion Thruster Performance Impacts Due to Cathode Wear. J Propuls Power 27(4):728. https://doi.org/10.2514/1.55011
52. Van Noord JL, Soulas GC, Sovey JS (2009) NEXT PM1R Ion Thruster and Propellant Management System Wear Test Results. Paper IEPC-2009-163, presented at the 31st International Electric Propulsion Conference, Ann Arbor, Michigan, 20–24 September, 2009
53. Tighe WG, Chien K-r, Solis Z, Spears R (2009) The 25 cm XIPS © Life Test and Post-Test Analysis. Paper IEPC-2009-161, presented at the 31st International Electric Propulsion Conference, Ann Arbor, Michigan, 20–24 September, 2009

Publisher's Note